UNIVERSITY OF THESSALY
SCHOOL OF ENGINEERING
DEPARTMENT OF MECHANICAL ENGINEERING

Diploma Thesis

Modeling of gas distribution systems over the whole range of the Knudsen number: application in the ITER primary vacuum system

by
NIKOLAOS VASILEIADIS

Submitted for the Partial Fulfillment
of the Requirements for the Degree of
Diploma in Mechanical Engineering
2016

Εγκρίθηκε από τα Μέλη της Τριμελούς Εξεταστικής Επιτροπής:

Πρώτος Εξεταστής (Επιβλέπων) — Δρ. Βαλουγεώργης Δημήτριος
Καθηγητής, Τμήμα Μηχανολόγων Μηχανικών, Πανεπιστήμιο Θεσσαλίας

Δεύτερος Εξεταστής — Δρ. Ανδρίτσος Νικόλαος
Καθηγητής, Τμήμα Μηχανολόγων Μηχανικών, Πανεπιστήμιο Θεσσαλίας

Τρίτος Εξεταστής — Δρ. Λυχναρόπουλος Ιωάννης
ΕΔΙΠ, Τμήμα Μηχανολόγων Μηχανικών, Πανεπιστήμιο Θεσσαλίας

Certified by the member of the Thesis Committee:

1st member (Supervisor) Dr. Valougeorgis Dimitrios
Professor, Department of Mechanical Engineering, University of Thessaly

2nd member Dr. Andritsos Nikolaos
Professor, Department of Mechanical Engineering, University of Thessaly

3rd member Dr. Lihnaropoulos Ioannis
LTP, Department of Mechanical Engineering, University of Thessaly

Acknowledgments

I would like to express my appreciation and gratitude to my supervisor Prof. Dimitris Valougeorgis for investing his trust and support to me and my work related to my thesis. His constant guidance and inspiration had a great impact in the quality of this thesis.

I would like to thank the members of the committee, Prof. Nikolaos Andritsos and Prof. Ioannis Lihnaropoulos for dedicating their time to read my thesis and provide supportive revisions. In addition, I am grateful to all my colleagues and friends in the laboratory of Transport Phenomena and Process Equipment for the stimulating and helpful scientific discussions we had.

I would also like to thank my parents, Ioannis Vasileiadis and Eleni Eleutheraki as well as my brother Neoklis. Without their support this endeavor would have never been possible. Finally, I would like to express special thanks to my friends for their selfless support.

Modeling of gas distribution systems over the whole range of the Knudsen number: application in the ITER primary vacuum system

Nikolaos Vasileiadis
University of Thessaly, Department of Mechanical Engineering, 2016

Supervisor: Valougeorgis Dimitrios, Professor, Department of Mechanical Engineering, University of Thessaly

Abstract

This work is focused in establishing a recently developed and enhanced numerical tool for modeling and simulating complex gas distribution systems that operate under any vacuum conditions. Such systems have lately received considerable attention due to their applicability and optimization potential in a vast number of industrial processes and technological applications. The wide range of pressures and characteristic lengths inside the network lead to conditions that are beyond the application of the classic Navier-Stokes theory, as the gas cannot be considered as a continuous medium and kinetic modeling is required.

At first the basic concepts of gas distribution systems and the governing equations such as the mass and energy conservation equations are examined and then the methodology for simulating such systems is presented and benchmarked. Then, the developed algorithm is applied to model the ITER primary pumping system. The boundary conditions of the network i.e. the pressures at the fixed grade nodes are taken to be constant, assuming steady-state conditions. Qualitative results for the flow patterns in the cassettes and along the divertor ring, as well as the throughputs for various operational scenarios in both the burn and dwell phases are presented and compared with existing results. The agreement with published results is found to be satisfactory considering the complexity of the problem and the fact that the presented and previously published approaches are based on different principals.

In addition, an explicit hybrid time integration method is introduced in this work in order to simulate time-dependent networks with minimal computational effort. The explicit coupling is justified by the time scale separation of the kinetic and macroscopic levels of the problem. The

hybrid coupling methodology is also benchmarked and applied to simulate the pump down of the ITER vacuum vessel between successive plasma shots as a transient problem.

This study is an additional step in a long-time effort towards establishing the developed integrated algorithm as a verified and promising computational tool for simulating gas distribution systems at any level of rarefaction.

Μοντελοποίηση δικτύων αγωγών αερίων σε όλο το εύρος του αριθμού Knudsen: Εφαρμογή στο σύστημα άντλησης του αντιδραστήρα σύντηξης ITER

Νικόλαος Βασιλειάδης
Πανεπιστήμιο Θεσσαλίας, Τμήμα Μηχανολόγων Μηχανικών, 2016

Επιβλέπων: Βαλουγεώργης Δημήτριος, Καθηγητής, Τμήμα Μηχανολόγων Μηχανικών, Πανεπιστήμιο Θεσσαλίας

Περίληψη

Η εν λόγω εργασία επικεντρώνεται στην παρουσίαση ενός πρόσφατα αναπτυγμένου αριθμητικού εργαλείου για την μοντελοποίηση και προσομοίωση πολύπλοκων δικτύων αγωγών αερίων που λειτουργούν κάτω από ποικίλες συνθήκες κενού. Τέτοια συστήματα έχουν λάβει τα τελευταία χρόνια ιδιαίτερη προσοχή λόγω της ευρείας εφαρμογής τους και των δυνατοτήτων βελτιστοποίησης που προσφέρουν σε ένα μεγάλο αριθμό βιομηχανικών διεργασιών και τεχνολογικών εφαρμογών. Το ευρύ φάσμα των πιέσεων και των χαρακτηριστικών μηκών στο εσωτερικό του δικτύου οδηγούν το αέριο σε συνθήκες που είναι πέρα από το πεδίο εφαρμογής της κλασικής θεωρίας Navier-Stokes, ενώ απαιτείται η χρήση κινητικής θεωρίας, καθώς το αέριο δεν μπορεί πλέον να θεωρηθεί ως συνεχές μέσο.

Αρχικά εξετάζονται οι βασικές έννοιες των συστημάτων διανομής αερίων και οι εξισώσεις που τα διέπουν, όπως οι εξισώσεις διατήρησης μάζας και ενέργειας ενώ έπειτα παρουσιάζεται και ελέγχεται η μεθοδολογία για την προσομοίωση των συγκεκριμένων συστημάτων. Στην συνέχεια, ο αλγόριθμος χρησιμοποιείται για την προσομοίωση του συστήματος άντλησης του αντιδραστήρα ITER. Οι οριακές συνθήκες του δικτύου στους κόμβους γνωστής πίεσης λαμβάνονται σταθερές, υποθέτοντας συνθήκες σταθερής λειτουργίας του αντιδραστήρα . Στην συνέχεια, παρουσιάζονται ποιοτικά αποτελέσματα για την ροή μέσα στα cassettes του αντιδραστήρα και κατά μήκος του τόρου, καθώς και οι προκύπτουσες μαζικές παροχές για διάφορα σενάρια λειτουργίας τα οποία συγκρίνονται με ήδη υπάρχοντα αποτελέσματα. Η συμφωνία με δημοσιευμένα αποτελέσματα είναι αρκετά ικανοποιητική

λαμβάνοντας υπόψη την πολυπλοκότητα του προβλήματος και το γεγονός ότι η προσέγγιση της παρούσας εργασίας διαφέρει από την αντίστοιχη δημοσιευμένη μεθοδολογία.

Επιπλέον, στο πλαίσιο της εργασίας προτείνεται μια ρητή υβριδική μέθοδος η οποία απαιτεί ελάχιστο υπολογιστικό φορτίο για την προσομοίωση δικτύων που λειτουργούν σε μη μόνιμες συνθήκες. Η εφαρμογή της παραπάνω μεθόδου δικαιολογείται από την μεγάλη διαφορά των χρονικών κλιμάκων που χαρακτηρίζουν το κινητικό και μακροσκοπικό επίπεδο του προβλήματος. Η συγκεκριμένη μέθοδος επαληθεύεται και εφαρμόζεται για την προσομοίωση του δικτύου του ITER ως πρόβλημα μη μόνιμων συνθηκών.

Η παρούσα μελέτη αποτελεί ένα επιπλέον βήμα στην καθιέρωση του κώδικα ως ενός υπολογιστικού εργαλείου για την προσομοίωση δικτύων διανομής αερίων που λειτουργούν σε οποιεσδήποτε συνθήκες αραιοποίησης.

Contents

Contents x
List of Figures xi
List of Tables xii
Chapter 1: Introduction 1
1.1 Introduction to gas distribution systems 1
1.2 The Knudsen number and flow regimes 2
1.3 Thesis structure and objectives 5
Chapter 2: Literature review 7
2.1 Rarefied pressure driven flows 7
2.2 Network solvers 12
2.3 Applications of vacuum gas distribution systems 15
Chapter 3: Gas distribution systems 17
3.1 Geometrical components 17
3.2 Governing equations 19
3.3 Identification of loops and pseudoloops 20
3.4 Integrated steady-state algorithm 23
3.5 Time dependent gas distribution systems – Hybrid scheme 25
3.6 Benchmarking 27
Chapter 4: The ITER primary vacuum pumping system 35
4.1 Geometry 35
4.2 Results of the ITER divertor primary pumping system 39
4.2.1 Burn Phase 40
4.2.2 Dwell Phase 47
4.2.3 Time-dependent 51
Chapter 5: Concluding remarks 55
References 56
Appendix A: Basic definitions in kinetic theory 60
Appendix B: Kinetic data for various flow setups 64

List of Figures

Figure 1: Pressure driven flow configuration 7
Figure 2: Geometrical components of an example network. 17
Figure 3: Extraction of loops in an example network. 22
Figure 4: Logic diagram of the integrated steady-state algorithm. 24
Figure 5: Transient example network. 25
Figure 6: First steady state benchmark network. 28
Figure 7: Second steady state benchmark network. 30
Figure 8: Pressure evolution for nodes 2, 8, 9 and 16 of the gas network shown in Fig. 7. 33
Figure 9: Mass flow rate evolution for pipes 1, 5, 6, 13 and 19 of the gas network shown in Fig. 7. 33
Figure 10: Comparison of pressure evolution inside the finite volume tank with the direct and hybrid schemes 34
Figure 11: View of the cross section along a cassette connected to a pump and schematic representation of the corresponding pipe network approximating the geometry of the actual gas flow path. 36
Figure 12: Schematic representation of the pipe network approximating the geometry of the actual gas flow between adjacent cassettes in the toroidal direction along the divertor ring and through the gaps between the cassettes facing the plasma side. 37
Figure 13: Direction of the gas flow in the pipe network simulating the actual gas flow path in the cross section along a cassette connected to a pump in the burn phase. 40
Figure 14: Direction of the gas flow in the pipe network simulating the actual gas flow path between adjacent cassettes in the toroidal direction along the divertor ring and through the gaps between the cassettes facing the plasma side in the burn phase. 41
Figure 15: Computed throughputs toward the pumps in the burn phase versus dome pressure with 4 pumps running and various gap widths; corresponding results in [48] are also included. 43
Figure 16: Computed throughputs toward the plasma in the burn phase versus dome pressure with 4 pumps running and various gap widths; corresponding results in [48] are also included. 44
Figure 17: Computed throughputs toward the pumps and the plasma in the burn phase versus dome pressure with 4 and 6 pumps running. 46
Figure 18: Direction of the gas flow in the pipe network simulating the actual gas flow path in the cross section along a cassette connected to a pump in the dwell phase. 48
Figure 19: Direction of the gas flow in the pipe network simulating the actual gas flow path between adjacent cassettes in the toroidal direction along the divertor ring and through the gaps between the cassettes facing the plasma side in the dwell phase. 49
Figure 20: Computed throughputs in the dwell phase versus dome pressure running with 4 (up) and 6 (down) pumps; corresponding results in [48] are also included 50
Figure 21: Vacuum vessel pressure distribution over the first 1000 s of the dwell phase for various initial conditions. 52
Figure 22: Vacuum vessel pressure at the end of the 1400 s dwell phase versus the initial outgassing rate with a decaying index n=-0.73 for various temperatures and pumping setups.... 53
Figure 23: Vacuum vessel pressure at the end of the 1400 s dwell phase versus the initial outgassing rate with a decaying index n=-0.73 for various temperatures and pumping setups.... 54

List of Tables

Table 1: Flow regimes with respect to the Knudsen number 3
Table 2: Fitting parameters of Eq. (2.2.4) for common tube cross sections 15
Table 3: Pressure [Pa] at the nodes of the sample network shown in Fig. 6. 29
Table 4: Tube mass flow rate [Kg/s] of the sample network shown in Fig. 6. 29
Table 7: Node numbers, length and diameter of all piping elements shown in Figs. 11 and 12.. 38
Table 8: Partial pressure [Pa] of deuterium (D2) at fixed pressure nodes for the three operating scenarios in the burn phase [48] 39
Table 9: Throughputs [Pa m3 s-1] for the three sensitivity analysis scenarios 45
Table 10: Throughputs [Pa m3 s-1] for various operating pump sequences for the 3000s non-inductive scenario in the low dome pressure (R denotes regeneration) 47
Table 11: Throughputs [Pa m3 s-1] for various operating pump sequences for the 3000s non-inductive scenario in the high dome pressure (R denotes regeneration). 47

Chapter 1: Introduction

1.1 Introduction to gas distribution systems

Internal flows in pipelines and ducts are commonly encountered in all parts of our industrialized society. From delivering natural gas and other industrial gases up to particle accelerators and fusion reactors, engineers have designed and constructed untold kilometers of relatively large-scale piping systems. Smaller piping units are also in abundance: in pneumatic controls, in heating and air conditioning systems, and in pulmonary flow systems, to name only a few. The governing equations for the simulation of such systems require the pressure drop inside a pipe to be expressed as a function of the flow rate or the gas velocity and thus pressure driven flows have been thoroughly investigated over the years.

One of the earliest and most widely used expressions being the Hagen-Poiseuille law, which was derived independently by Gotthilf Heinrich Ludwig Hagen in 1839 and Jean Léonard Marie Poiseuille in 1838, and published by Poiseuille in 1840 and 1846:

$$\frac{\Delta P}{\Delta L} = \frac{32\mu\bar{u}}{D^2} \tag{1.1}$$

Pressure driven flow results through tubes were then expanded from laminar to turbulent conditions by the Darcy-Weisbach equation which relates the pressure loss due to friction along a given pipe length to the average velocity of the gas. The Darcy-Weisbach equation contains a dimensionless friction factor known as the Darcy friction factor, which was plotted against the Reynolds number for various values of the relative roughness by Lewis Ferry Moody to publish the widely known Moody's diagram, in 1944.

However, in many gas distribution processes the conveying gas rarefaction ranges from the free molecular up to the hydrodynamic limit and thus these flows must be tackled by kinetic theory. Kinetic theory approaches the gas as a huge amount of atoms moving randomly in all directions colliding with each other, rather than a continuous medium as in classic fluid dynamics. Kinetic modeling can be successfully implemented to study rarefied pressure driven

flows and obtain similar results with those described above for the pressure drop of a rarefied gas along a tube. Finally, using the above results simulation of gas distribution systems can be extended to the whole range of gas rarefaction

1.2 The Knudsen number and flow regimes

In rarefied gas flows the parameter that characterizes the flow is the Knudsen number Kn introduced around 1909 [1], defined as:

$$Kn = \frac{\lambda}{L} \tag{1.2.1}$$

where λ is the mean free path of the gas, defined as the average distance that gas particles travel between successive collisions and L is the characteristic length of the problem. In many cases it is necessary to define the Knudsen number as:

$$Kn = \frac{\lambda}{\varphi}\left|\frac{d\varphi}{dx}\right| \tag{1.2.2}$$

where φ is a flow quantity. The later definition of the Knudsen number is more general and can locally characterize the flow rarefaction. For the Hard Sphere model and for a single monoatomic gas the mean free path can be expressed as [2]:

$$\lambda = \frac{m}{\sqrt{2}\pi d^2 \rho} \tag{1.2.3}$$

where m is the molecular mass, d is the diameter of the molecule and ρ is the mass density of the gas. The Knudsen number can also be expressed by the widely known Mach (Ma) and Reynolds (Re) numbers as:

$$Kn = \sqrt{\frac{\pi\gamma}{2}} \frac{Ma}{\mathrm{Re}} \tag{1.2.4}$$

where γ is the specific heat ratio of the gas. Alternatively, instead of the Knudsen number the rarefaction parameter is also commonly used:

$$\delta = \frac{PL}{\mu u_0} = \frac{\sqrt{\pi}}{2Kn} \tag{1.2.5}$$

where P is the gas pressure, μ is the absolute viscosity, $u_0 = \sqrt{2k_B T / m}$ is the most probable velocity and k_B the Boltzmann constant. Both the Knudsen number and rarefaction parameter are measures of gas rarefaction and departure from local equilibrium. According to the Knudsen number the flow regimes can be defined as shown in Table 1.

Table 1: Flow regimes with respect to the Knudsen number

Range of Kn	Flow regime	Governing Equations	Numerical approach
$Kn \to 0$	Continuum (inviscid)	Euler	Typical CFD schemes
$Kn < 10^{-3}$	Continuum (viscous)	Navier Stokes	
$10^{-3} < Kn < 10^{-1}$	Slip (viscous)	Navier Stokes with Slip boundary conditions, Generalized equations	
$10^{-1} < Kn < 10$	Transition (Knudsen)	Boltzmann Kinetic models	Analytical methods, Variational methods, Discrete Velocity Method, Integro-Moment Method Direct Simulation Monte Carlo

$10 < Kn$	Free molecular	Boltzmann and kinetic models without collisions	Method of characteristics, Test Particle Monte Carlo

When the Knudsen number is small and the flow is in the continuum regime and the Euler and Navier Stokes equations with no slip boundary conditions can be used with high accuracy. As the Knudsen number is increased and the flow moves to the slip regime, the no slip boundary conditions do not hold and thus velocity slip and temperature jump boundary conditions [3] must be applied alongside with the Navier Stokes approach. As the Knudsen number is further increased and the flow enters the transition and free molecular regimes the Newton, Fourier and Fick transport laws fail and the continuum approach collapses. It is in those regimes that non equilibrium phenomena appear and the flow can only be simulated by kinetic theory [4, 5].

The Boltzmann equation, while valid in all flow regimes, is utilized only in the free molecular up to the transition regime due to the high computational cost involved. The direct solution of the Boltzmann equation is a very computationally demanding process and thus certain methods have been developed to overcome this. One of them is the use of kinetic models which deterministically replace the collision part of the Boltzmann equation. In order for a model to be accepted it must satisfy the collision invariants, the H-theorem and provide the correct values for the transport coefficients. The most well-known kinetic models are the BGK [6], the Shakhov [7] and the Ellipsoidal [8] models for monoatomic single gases, the Holway [9] and Rykov [10] models for polyatomic single gas flows and the McCormak [11] model for gas mixtures. The formulation of the Boltzmann equation and the BGK model are presented in Appendix A for completeness.

Another method developed to overcome the direct solution of the Boltzmann equation is the Direct Simulation Monte Carlo method [12]. In this stochastic method the flow domain is discretized and a number of simulating particles is distributed inside with each particle simulating a large number of real particles. The real motion of the particles is divided into two parts. The first part is the free motion of the particles calculated by their respective velocities and the time step, while the second part is the collision of the particles which is simulated

stochastically. Then, the macroscopic quantities of interest are calculated using the simulator particles which are sampled for a large number of time steps. It is noted that like all stochastic methods the DSMC suffers from statistical noise, especially in creeping flows.

1.3 Thesis structure and objectives

The simulation of gas distribution systems has always been a popular field of engineering due to its vast applicability and optimization potential in industrial and technological processes. Recently the growing development of large vacuum systems has constituted the ability to simulate such systems mandatory. Thus, the thesis aim is to establish a recently developed and enhanced numerical tool for simulation of gas distribution systems operating under any vacuum conditions. In addition, the introduced algorithm is implemented to simulate various steady state and transient scenarios of the ITER primary vacuum system. ITER is an experimental fusion reactor which is under construction in Cadarache, France [13] and its vacuum systems are considered as the most complex ones worldwide. The thesis is outlined as follows:

- In Chapter 2 the literature review is presented. It includes the linear and nonlinear solutions of pressure driven flows through tubes of circular cross section as well as the end effect theory. Methodologies already applied to simulate gas networks in all flow regimes and the most widely known applications of such systems are also presented.

- In Chapter 3 an introduction to the basic concepts and governing equations of gas distribution systems is included. The principals, methodologies and structures of both the steady state and transient algorithms developed are also included here. Finally, benchmark results for a total of three networks operating under rough vacuum are provided for both algorithms to ensure their validity.

- In Chapter 4 the ITER divertor system geometry is studied initially and then various operation scenarios are simulated. The operational scenarios include the simulation of the burn and dwell phase at steady conditions and both qualitative and quantitative results are

presented. The simulation of the dwell phase as a transient problem using an explicit coupling method is also examined here.

- In Chapter 5 a summary of the thesis with the corresponding concluding remarks are presented.

Chapter 2: Literature review

2.1 Rarefied pressure driven flows

Over the years rarefied single gas pressure driven flows through circular tubes have attracted considerable attention due to their wide applicability in industrial processes and technological applications operating in the whole range of the Knudsen number. The proposed methodology of simulating gas distribution systems operating under rarefied conditions includes the computed mass flow rates through single pipe elements, which are stored in a data base for the needs of the network algorithm and thus a literature survey of pressure driven flows is deemed necessary. In most cases , the flow is numerically solved either stochastically based on the DSMC method or deterministically based on the kinetic modeling by directly solving the Boltzmann equation or based on suitable kinetic models as described in Chapter 1. Very good agreement between corresponding results obtained by all methods has been observed across all flow regimes for tubes of various lengths over radius ratios as well as for various pressure ratios. Moreover, computational results match very well to available experimental data.

The flow configuration of a pressure driven flow as shown in Fig. 1 is well known but it is also described here for completeness and clarity. Consider two vessels that are connected by a tube of length L and radius R and are maintained at constant pressures P_A, P_B and temperatures T_A, T_B with $P_A > P_B$ and $T_A = T_B$.

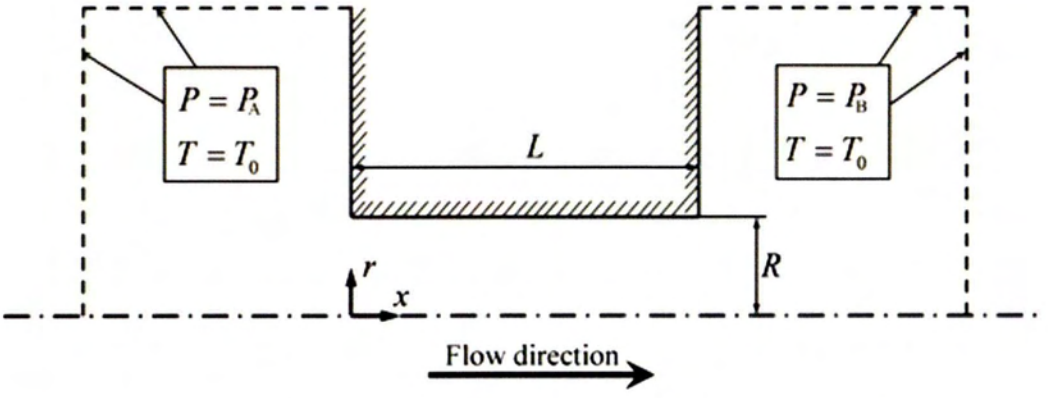

Figure 1: Pressure driven flow configuration

Due to the pressure difference of the two reservoirs there is an axisymmetric flow in the axial direction with the macroscopic quantities varying in the axial and radial directions. At the open boundaries (dotted lines) the gas is at rest and the incoming distributions are the local Maxwellian ones. The volume of the two reservoirs is taken large enough to justify the boundary conditions implemented. At the tube walls (solid lines) purely diffusive gas surface interaction is considered while along the symmetry axis at $\hat{r}=0$ purely specular reflection is considered. The flow configuration is a five dimensional one (two dimensions in the physical space and three in the molecular velocity space) and is defined by three dimensionless parameters: the reference gas rarefaction parameter, the pressure ratio and the aspect ratio denoted as $\delta_A = P_A R/\mu_A u_A$, P_B/P_A and L/R respectively. Although the flow configuration seems quite simple the computational effort required to solve the nonlinear problem is considerable and thus linearization is performed to save computational resources.

For very long tubes $L/R >> 1$ the infinite capillary theory, where the flow is considered as fully developed, can be applied. Pressure is assumed to vary only in the flow direction and thus only a cross section of the tube must be solved. Extensive tabulated results for the non-dimensional flow rate $G_{FD}(\delta)$ may be easily found in the literature [14]. In addition, a highly accurate interpolation formula has been recently introduced [15]:

$$G_{FD}(\delta) = \frac{1.505 + 0.0524\delta^{0.75}\ln\delta}{1+0.738\delta^{0.78}} + \left(\frac{\delta}{4}+1.018\right)\frac{\delta}{1.073+\delta} \qquad (2.1.1)$$

Following a well-known procedure the mass flow rate is written as:

$$\dot{M}_{FD} = \frac{\pi R^3}{\upsilon_A}\frac{\Delta P}{L}G^* \qquad (2.1.2)$$

where

$$G^* = \frac{1}{\delta_A - \delta_B}\int_{\delta_A}^{\delta_B} G_{FD}(\delta)d\delta \qquad (2.1.3)$$

is computed by integrating $G(\delta)$ between the inlet and outlet rarefaction parameters δ_A and δ_B respectively accordingly defined by the corresponding pressures P_A and P_B. Moreover, it has been shown that in the case of circular tubes the integration procedure is not necessary and G^* can be simply computed with high accuracy as:

$$G^* = G\left(\frac{\delta_A + \delta_B}{2}\right) \tag{2.1.4}$$

The assumption of a fully developed flow significantly reduces the computational cost. However, the assumption of fully developed flow is not always fulfilled in practice, leading to a significant error in flow rate estimation because of the capillary inlet and outlet influence. For medium capillaries, the end effects can be taken into account by introducing the concept of the effective length, i.e. the real capillary L length is corrected by an additional length ΔL. The end effect correction was initially calculated for slow viscous flows [16] and then the same idea was used for rarefied gas flows through moderately long channels [17, 18]. Once the end effect corrections at both the inlet and the outlet regions have been calculated the reduced flow rate through the capillary can be computed as:

$$G^* = \frac{1}{1 + \Delta L_{in}/L + \Delta L_{out}/L} \frac{1}{\delta_A - \delta_B} \int_{\delta_A}^{\delta_B} G_{FD}(\delta) d\delta \tag{2.1.5}$$

or by introducing Eq. 2.1.4 as:

$$G^* = \frac{1}{1 + \Delta L_{in}/L + \Delta L_{out}/L} G\left(\frac{\delta_A + \delta_B}{2}\right) \tag{2.1.6}$$

As described in [19] the end effect corrections can be computed directly, i.e. only the inlet and outlet regions are considered using the fully developed flow as the boundary condition. The knowledge of this quantity circumvents the solution of the complete problem and reduces significantly the computational effort without the loss of accuracy. The idea is similar to that

applied to the velocity slip and temperature jump problems [20], where only the Knudsen layer is considered using the asymptotic behavior in the gas bulk as the boundary condition. Following the above procedure the length corrections ΔL_{in}, ΔL_{out} can be calculated as a function of only the rarefaction parameter at the inlet and outlet of the tube and are presented in Appendix B. In addition, a formula that interpolates the above data with a maximum deviation of 0.8% has been deduced:

$$\frac{\Delta L}{R} = 0.68 + \frac{1.399}{\delta^{0.042} Exp(0.677\delta) + 2.950\delta^{0.631}} \tag{2.1.7}$$

The great advantage of the infinite capillary and end effect theory is that the dimensionless solutions solely depend on the gas rarefaction parameter and not on the pressure and aspect ratios. However, both theories are based on linear kinetic analysis and are valid when specific criteria hold [21]. To satisfy this requirement and after some extensive numerical experimentation the mass flow rate is obtained according to the above analysis provided that $L/R \geq 10$ and the inlet rarefaction parameter $\delta \leq 100$.

In the case of $L/R < 10$ and if the pressure ratio is small i.e. $P_B/P_A > 0.9$ the flow can be considered as linear even in short tubes and the solution is obtained by solving the linearized BGK equation in the whole flow field instead of a cross section [22]. The mass flow rate is obtained by:

$$\dot{M}_{LIN} = \frac{W_{LIN}\sqrt{\pi}R^2(\mathrm{P_A} - \mathrm{P_B})}{u_0} \tag{2.1.8}$$

where the dimensionless flow rate W_{LIN} is computed from the velocity field inside the tube as:

$$W_{LIN} = 4\sqrt{\pi}\int_0^1 u_z(r,z)\,r dr \tag{2.1.9}$$

The dimensionless flow rate W_{LIN} is calculated in terms of the rarefaction parameter δ and the aspect ratios of the tube. It is obvious that the computational effort is reduced solely on the fact

that with the linearization of the flow the pressure ratio P_B/P_A parameter is eliminated. Indicative results of W_{LIN} are provided in Appendix B.

If the criteria described above do not hold i.e. if $L/R \leq 10$ and $P_B/P_A \leq 0.9$ the flow is considered as nonlinear and must be tackled based either on the Direct Simulation Monte Carlo method [23, 24] or on nonlinear kinetic model equations solved by the parallelized discrete velocity method [25-27]. The mass flow rate through the tube is obtained by:

$$\dot{M}_{NL} = \frac{W_{NL}\sqrt{\pi}R^2 \mathrm{P_A}}{u_0} \tag{2.1.10}$$

where W_{NL} is the dimensionless nonlinear flow rare that depends on all three flow parameters described above (δ, L/R and P_B/P_A). The pressure difference between the inlet and the outlet of the tube is then given by:

$$\mathrm{P_A} - \mathrm{P_B} = \mathrm{P_A}\left(1 - \frac{\mathrm{P}_B}{\mathrm{P}_A}\right) = \frac{\dot{M}_{NL}u_0}{W_{NL}\sqrt{\pi}R^2}\left(1 - \frac{\mathrm{P}_B}{\mathrm{P}_A}\right) \tag{2.1.11}$$

It is obvious that this case is the most computationally demanding one and extensive computations have been performed to prepare an adequate large and dense data base over a wide range of the involved parameters. Indicative results of are reported at Appendix B.

The results and formulas provided by both linear and nonlinear kinetic theory are used in order to have an explicit expression of the pressure drop inside a tube as a function of the flow rate for all flow parameters. The above can be used to develop a gas distribution system solver in the whole range of the Knudsen number as it will be described below. In order to decrease computational effort only pressure driven flows through circular tubes are considered in this work. In the case of channels with arbitrary cross section the flow is simulated by converting the noncircular cross section to an equivalent circular one based on two different approaches. In the first approach the radius of the equivalent circular channel is defined according to the hydraulic radius concept [28], while in the second one it is defined by equating the areas of the noncircular and circular cross sections [29].

2.2 Network solvers

A survey of algorithms that have been already developed in the past years for modeling gas networks is provided. In the hydrodynamic regime computational algorithms dedicated to the hydraulic design and optimization of gas pipe networks (e.g. compressed air, natural gas, etc.) are well established [30-35] and widely available. Such software is the Pipe2016 computational package that has been under development since 1973 from the University of Kentucky [36]. Pipe2016 analyzes, one-dimensional, isothermal flow for ideal and non-ideal variable density gases and can accommodate large networks, looped systems and multiple load and supply points. In addition, several scenarios can be set up in a single model such as load or supply changes and open or closed valves. Pipe2016 offers an integrated GUI from which the user can provide all the required input data such as the piping elements length and diameter, pipe fittings (e.g. bends, T's, reducers, etc.), node load or supply as well as compressors and fans. For the simulation of the gas network the linear pressure loss at each tube is taken from the Darcy-Weisbach equation as

$$\Delta P = f_D \frac{L}{D} \frac{\rho V^2}{2} \tag{2.2.1}$$

where f_D is the Darcy friction factor, L and D are the length and diameter of the pipe, while ρ and V are the mean density and velocity of the gas inside the pipe. The Darcy friction factor is calculated from well-known empirical expressions and depends on the characteristics of the flow inside the tube. The pressure loss due to pipe fittings is given following the K-method [37] as:

$$\Delta P = K \frac{\rho V^2}{2} \tag{2.2.2}$$

where K is the resistance coefficient taken from the software's integrated libraries. For the description of the pressure-temperature relation inside the network the Ideal Gas law, while Non-Ideal Gas and Constant Density Gas analyses are also available.

In the free molecular regime particle collisions are negligible and thus the collision part of the Boltzmann equation is neglected. These types of flows are usually solved stochastically by using the Test Particle Monte Carlo method (TPMC). The TPMC closely resembles the DSMC

method by excluding the collisions between particles. The flow domain is discretized only at its boundaries and no internal discretization is required. Initially a large number of simulating particles is distributed at the domain boundaries with each particle simulating a large number of real molecules. Then, the simulating particles stochastically move inside the flow domain following rectilinear trajectories and can only collide with the domain's boundary surfaces. Depending on the type of boundary that a particle collides with, the particle can then be reflected either specularly or diffusively, absorbed by the surface or removed from the flow domain if the boundary is an open surface. Because the movement of particles is independent of each other, the TPMC method can be easily parallelized and thus it can provide fast results. It can be readily seen that the Test Particle Monte Carlo can be used to simulate gas distribution systems that operate at free molecular conditions. One of the most popular and widely available computational tools for molecular flow simulations is Molflow+ that has been under continuous development and addition of new features at CERN since 1991 [38]. For the simulation of gas distribution systems the user must provide the network geometry through CAD programs and thus pipes with arbitrary cross sections and fittings can be geometrically represented with high accuracy. Gas tanks and pumps can be implemented with specific boundary surfaces while supplies or demands at certain points of the network can also be given. In addition, Molflow+ offers the capability of transient simulations which can be of major importance in gas networks analysis.

Recently, ITERVAC a numerical tool for gas network simulations has been developed at the Karlsruhe Institute of Technology (KIT) for gas network calculations in the whole range of the Knudsen number [39]. The input data are provided through a GUI that allows the user to build 2D networks. Then, ITERVAC uses semi-empirical expressions to determine the mass flow rates inside a pipe as a function of the corresponding pressure drop between the hydrodynamic and free molecular limits. The expression for the flow rate is given as:

$$\dot{M} = F \frac{\pi D_h^3}{8 u_0} \frac{\partial P}{\partial x} \tag{2.2.3}$$

where D_h is the hydraulic diameter of the tube $u_0 = \sqrt{2 k_B T / m}$ is the most probable velocity and F is given as a function of four fitting parameters:

$$F = \frac{C_1}{Kn} + C_2 + \frac{C_3 Kn}{C_4 + Kn} \tag{2.2.4}$$

Taking the limit of Eq. (2.2.4) in the viscous regime ($Kn \to 0$) the value C_1 of can be determined as:

$$\lim_{Kn \to 0} F = \frac{C_1}{Kn} = F_{visc} \Rightarrow C_1 = \frac{4\sqrt{\pi}}{f_D \,\mathrm{Re}} \tag{2.2.5}$$

where f_D is the Darcy friction factor and Re is the Reynolds number. A more general approach is to take C_1 as:

$$C_1 = \frac{C_{lam} 16A}{\sqrt{\pi} D_h^2 \,\mathrm{Re}\, f_D} \tag{2.2.6}$$

Taking the limit of Eq. (2.2.4) in the free molecular regime ($Kn \to \infty$) the following expression for the fitting parameters parameters C_2 and C_3 can be obtained:

$$\lim_{Kn \to \infty} F = C_2 + C_3 = F_{mol} \tag{2.2.7}$$

Assuming an isothermal, isotropic Maxwellian distribution inside a circular channel Eq. (2.2.7) becomes:

$$C3 + C4 = \frac{2W}{\sqrt{\pi}} \frac{L}{D} \tag{2.2.8}$$

where W is the dimensionless free molecular flow rate through the circular tube. The remaining fitting parameter C_4 is taken as a fixed parameter that describes the beaming effects. Values for the four coefficients are presented for some common tube cross sections in Table 2.

Table 2: Fitting parameters of Eq. (2.2.4) for common tube cross sections

Geometry	C_{lam}	C_2	C_3	C_4
Circular	1.000	1.116	0.329	1.400
Rectangular (1x1)	1.124	1.486	0.574	1.400
Rectangular (2x1)	1.029	1.666	0.732	1.400
Triangular	1.200	1.340	0.963	1.400

For short channels $(L/D_h < 80)$ C_2 and C_3 are weighted by a correction factor while C_1 is corrected for entrance and exit effects. Extensive computational and experimental benchmarking of ITERVAC's empirical expressions has been performed, with a highest deviation of 3% at the viscous and free molecular regimes, increasing up to 40% for the transition regime.

2.3 Applications of vacuum gas distribution systems

As already mentioned many technological applications can be modeled as gas networks or require the utilization of some kind of gas distribution system. Typical examples include micro-filtering processes, flows through porous media, vacuum chambers for CD/DVD metallization and chip fabrication. Two of the largest vacuum systems are found at the Large Hadron Collider (LHC) located near Geneva in the France–Switzerland border and the ITER experimental fusion reactor now under construction in Cadarache, France.

The first start-up of LHC in 2008 constituted it as the biggest operational vacuum system in the world, operating at a variety of pressure levels and using an impressive array of vacuum technologies. The LHC features three separate vacuum systems: one for the beam pipes, one for insulating the cryogenically cooled magnets and one for insulating the helium distribution line. The first system is used to avoid the collisions of molecules inside the accelerator while the two later ones are used as a thermal insulator for the cryomagnets and the helium line. The three separate vacuum systems sum up to in a total of 104 kilometers of piping. The insulating vacuum

equivalent to some 10^{-4} Pa is made up of an impressive 50 km of piping while the remaining 54 km of pipes under vacuum are the beam pipes with a pressure level in the order of 10^{-9} up to 10^{-8} Pa. Due to the ultra-high vacuum conditions met at the LHC molecular flow conditions are assumed and thus Molflow+ has been used for simulating the three separate vacuum systems.

The successful operation of the ITER fusion reactor requires the constant conditioning and monitoring of the vacuum vessel. With a volume of 1400 m^3 and 8500 m^3 respectively, the ITER vacuum vessel and cryostat range amongst the largest vacuum systems ever to be built. Vacuum pumping is required prior to starting the fusion reaction to eliminate all sources of organic molecules that would otherwise be broken up in the hot plasma. Vacuum pumping is also required to create low density about one million times lower than the density of air. Mechanical pumps and powerful cryogenic pumps evacuate the air out of the vessel and the cryostat until the pressure inside has dropped to one millionth of normal atmospheric pressure. Considering the volume of ITER, this operation will take 24 to 48 hours. The main pumping systems are the six torus exhaust pumps, the four cryopumps for the neutral beam injection systems used in plasma heating, and the two cryopumps for the ITER cryostat to maintain the low pressure required for the operation of the superconducting magnets. Due to ITER's wide vacuum conditions ranging from the free molecular up to the slip regime a numerical tool that can simulate gas distribution systems in the whole range of the Knudsen number is required.

Chapter 3: Gas distribution systems

3.1 Geometrical components

It is worthwhile to examine the geometrical components that compose a typical network. A gas distribution system can be considered as a directed linear graph consisting of a finite number of nodes and pipes and the solution of the above graph consists of the pressure in each node and the mass flow rate in each pipe. Nodes are divided into two categories: inner and fixed grade nodes. Inner nodes have an unknown pressure but are allowed to have a demand in flow rate while fixed grade nodes have a known pressure and cannot have a demand in flow rate. A pipe on the other hand describes the adjacency between two nodes of the network and is characterized by its length L, and diameter D. The above two components are considered as the primary ones, as they can fully define any network. However, secondary geometrical components that consist of primary ones can be defined, such as the loops and the pseudoloops of the network. A loop is a closed pipe path, while a pseudoloop is a pipe path connecting two fixed grade nodes. According to graph theory for a well-defined network that consists of p pipes, n inner nodes, f fixed grade nodes and l loops the following relation must hold:

$$p = n + l + (\mathrm{f} - 1) \tag{3.1.1}$$

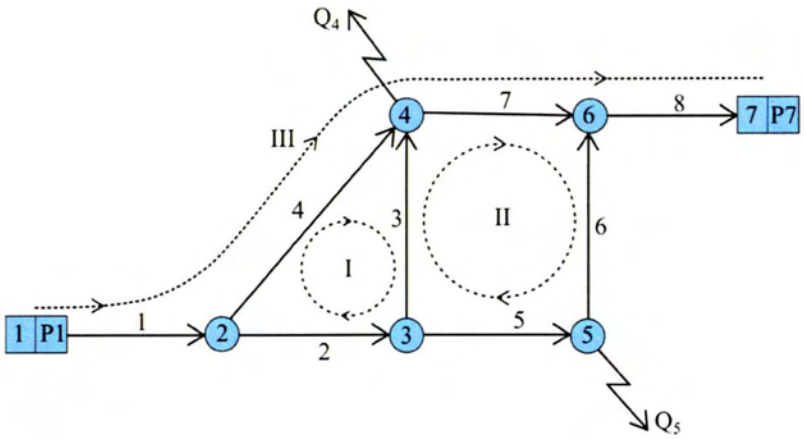

Figure 2: Geometrical components of an example network.

To clarify each component an example network is shown in Fig. 2. The above network consists of 7 nodes {1,2,3,4,5,6,7} from which 5 are inner nodes {2,3,4,5,6} and 2 are fixed grade nodes {1,7} and 8 pipes describing the connections between nodes {1-2, 2-3, 3-4, 2-4, 3-5, 5-6, 4-6, 6-7}. Also 2 loops and 1 pseudoloop can be defined respectively by their pipe paths {2-3-4, 3-5-6-7}, {1-4-7-8}. Assuming that the pressure drop in each pipe i is a function of the mass flow rate denoted by $F(M_i)$ then the system of equations is as follows:

1. Energy balance equations for each piping element:

$$\begin{aligned} P_1 - P_2 &= F(\mathrm{M}_1) & \qquad P_3 - P_5 &= F(\mathrm{M}_5) \\ P_2 - P_3 &= F(\mathrm{M}_2) & \qquad P_5 - P_6 &= F(\mathrm{M}_6) \\ P_3 - P_4 &= F(\mathrm{M}_3) & \qquad P_4 - P_6 &= F(\mathrm{M}_7) \\ P_2 - P_4 &= F(\mathrm{M}_4) & \qquad P_6 - P_7 &= F(\mathrm{M}_8) \end{aligned} \tag{3.1.2}$$

2. Mass continuity equations for each inner node:

$$\begin{aligned} M_1 - M_2 - M_4 &= 0 \\ M_2 - M_3 - M_5 &= 0 \\ M_3 + M_4 - M_7 &= Q_4 \\ M_5 - M_6 &= Q_5 \\ M_6 + M_7 - M_8 &= 0 \end{aligned} \tag{3.1.3}$$

Solving the 13 equations described above will provide the 13 unknown quantities of the network i.e. the 5 pressure values at each inner node and the 8 mass flow rates at each pipe. In order to use an iterative numerical scheme to solve this problem it is necessary to reduce the initial set of equations to a system that only contains the unknown mass flow rates. This can be achieved by combining the energy balance equations along the secondary geometrical components of the network. Thus, for the 2 loops of the system the energy balance equations are given as:

$$\begin{aligned} -F(M_2) + F(M_4) - F(M_3) &= 0 \\ F(M_3) + F(M_7) - F(M_6) - F(M_5) &= 0 \end{aligned} \tag{3.1.4}$$

For the pseudoloop of the network the energy balance equation is:

$$F(M_1)+F(M_4)+F(M_7)+F(M_8)=P_1-P_7 \tag{3.1.5}$$

For the loops and pseudoloops equations the flow is considered positive if the direction of its corresponding pipe agrees with the direction in which the loop or pseudoloop is defined, otherwise the flow is considered negative. The reduced set of equations is given as follows:

$$\begin{aligned}
-F(M_2)+F(M_4)-F(M_3)&=0\\
F(M_3)+F(M_7)-F(M_6)-F(M_5)&=0\\
F(M_1)+F(M_4)+F(M_7)+F(M_8)&=P_1-P_7\\
M_1-M_2-M_4&=0\\
M_2-M_3-M_5&=0\\
M_3+M_4-M_7&=Q_4\\
M_5-M_6&=Q_5\\
M_6+M_7-M_8&=0
\end{aligned} \tag{3.1.6}$$

It is observed that the initial set of 13 equations is reduced to 8. The reduced system of equations is linear and can be solved by Gauss elimination for the unknown flow rates.

3.2 Governing equations

As described above the governing equations consist of the mass conservation equations at each inner node and the energy balance equations at each loop and pseudoloop of the network. Thus a generalized set of governing equations can be determined for any network. The mass conservations equations are expressed as:

$$\left[\sum_j(\pm)\dot{M}_j-Q\right]_i=0 \tag{3.1.7}$$

where the index $1 \le i \le n$ refers each of the n inner nodes of the network, while the summation index j refers to the pipes connected to node i. The sign of the flow rate is taken positive or negative when the flow is into or out of the node respectively. The energy balance equations for the closed loops of the network are described as:

$$\left[\sum_{j}(\pm)\Delta \mathrm{P}_{j}\right]_{k}=0 \tag{3.1.8}$$

where the index $1 \le k \le l$ denotes the closed loops of the network, while the summation index refers to the pipes that constitute the loop k. The pressure drop is taken positive if the direction of pipe j agrees with the direction that loop k is defined, otherwise it is taken as negative. The energy balance equations for the pseudoloops connecting two fixed grade node of the network are given by:

$$\left[\sum_{j}(\pm)\Delta \mathrm{P}_{j}+\Delta H\right]_{m}=0 \tag{3.1.9}$$

where the index $1 \le m \le f-1$ refers to the $f-1$ pseudoloops of the network, while the summation index j refers to the pipes that constitute pseudoloop m and ΔH is the pressure difference between the two fixed grade nodes connected via pseudoloop m. Here again the pressure drop is taken positive if the direction of pipe j agrees with the direction in which pseudoloop m is defined, otherwise it is taken as negative. Based on the above the final generalized system of equations will consist of $n+l+f-1$ equations that can be solved for the unknown p mass flow rates according to relation 3.1.1.

3.3 Identification of loops and pseudoloops

As described, with the use of the closed loops and pseudoloops of the network the initial system of equations can be reduced to a set of equations that contains only the unknown flow

rates. For the identification of the l loops and $f-1$ pseudoloops of the network the well-known Depth First Search algorithm [40] is used. The DFS is an algorithm for searching or traversing tree and graph structured data. The algorithm starts from an arbitrary node and traverses the network through the pipe connections until all nodes have been travelled once.

Thus, the implementation of the algorithm in order to identify a set of $f-1$ independent pseudoloops of the network is straightforward. The DFS procedure starts from the first fixed grade node and traverses the graph until another fixed grade node is found. When this criterion is met the path between the two nodes is stored and the above procedure is repeated until all remaining fixed grade nodes have been found. This will always result in an independent set of $f-1$ pseudoloops, provided that the network is well defined.

On the other hand, the identification of a set of l independent loops is much more complicated. The DFS algorithm can be easily used to arbitrary identify loops from a given network, however the closed loops extracted by this procedure are not guaranteed to be linearly independent. The computational effort to check the independence of this extracted set of loops is formidable if not prohibitive. Thus, a "spanning tree" method [41] must be implemented. In the present work, two successive DFS algorithms are used to implement the spanning tree method. The first DFS algorithm starts from an arbitrary node and traverses the whole network via the pipe connections. At each node the algorithm checks for pipes that connect the current node with nodes that have been already visited. If such pipes exist they are deleted from the initial network and are stored in an adjacency array. After the first DFS procedure has been completed l pipes will have been deleted and the remaining network will have been reduced to a tree network that contains no loops. Then, each pipe deleted is individually added back to the tree network which now will contain a single loop. A second DFS algorithm is implemented to extract and store the pipe path of this single loop and the pipe element that has been added is again deleted. The above procedure is repeated for all the pipes stored and will always provide an independent set of l closed loops, given a well-defined network.

An example of the loop extraction procedure is shown in Fig. 3. In this case the first DFS algorithm will start at node {1} and will then visit nodes {2,3,4}. At node {4} a pipe connecting node {4} with a previously visited node, namely node {2} is found and thus it is deleted from the network. The DFS will continue to visit nodes {6,5} and will delete the pipe connecting nodes {5} and {3}. From node {5} the algorithm will backtrack to node {6} and will stop by traversing

to node {7} as all nodes of the network have been visited once. Then, pipe {2-4} will be added back to the network and a DFS procedure will start from node {2} to extract loop {I}. Pipe {2-4} is then deleted and the procedure is repeated for pipe {3-5} in order to extract loop {II}. The procedure stops when all the deleted pipes have been processed.

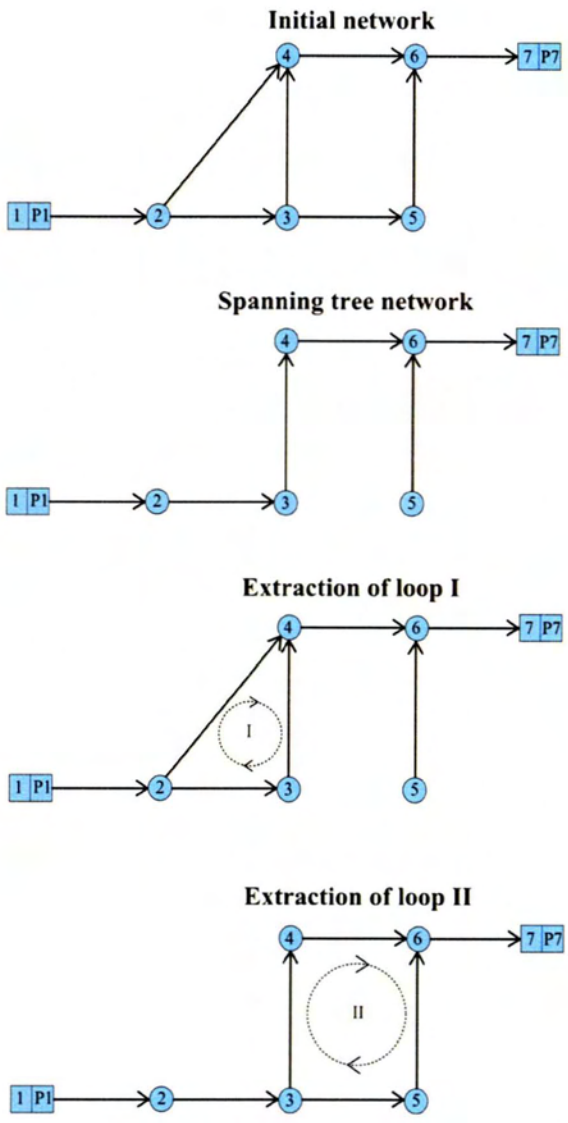

Figure 3: Extraction of loops in an example network.

3.4 Integrated steady-state algorithm

For the initialization of the integrated steady-state code the input data must be provided. The input data are the geometrical components of the network (inner nodes, fixed grade nodes, pipe elements) and the operational data (demand at each inner node, pressure at each fixed grade node, length and diameter of each piping element). Once the geometrical and operational data are provided an iterative procedure between the pressure drop equations and the network's mass and energy balance equations is implemented:

1. At all inner nodes of the network, pressure values are assumed and the pressure difference in each tube is calculated.

2. The closed loops and pseudoloops of the network are identified.

3. The rarefaction parameter at each pipe end is estimated.

4. The values of the dimensionless flow rates for each tube are interpolated from the available kinetic data bases.

5. The system of mass and energy balance equations (3.1.7), (3.1.8), (3.1.9) is solved by applying the Gauss elimination with partial column pivoting to compute the mass flow rates at each tube.

6. Pressure drop equations (3.1.2) are used to update the pressure at each inner node.

7. The updated pressure values are compared with the ones in Step 3 and the procedure is iterated upon convergence.

A detailed logic diagram of the steady-state algorithm is shown in Fig. 4.

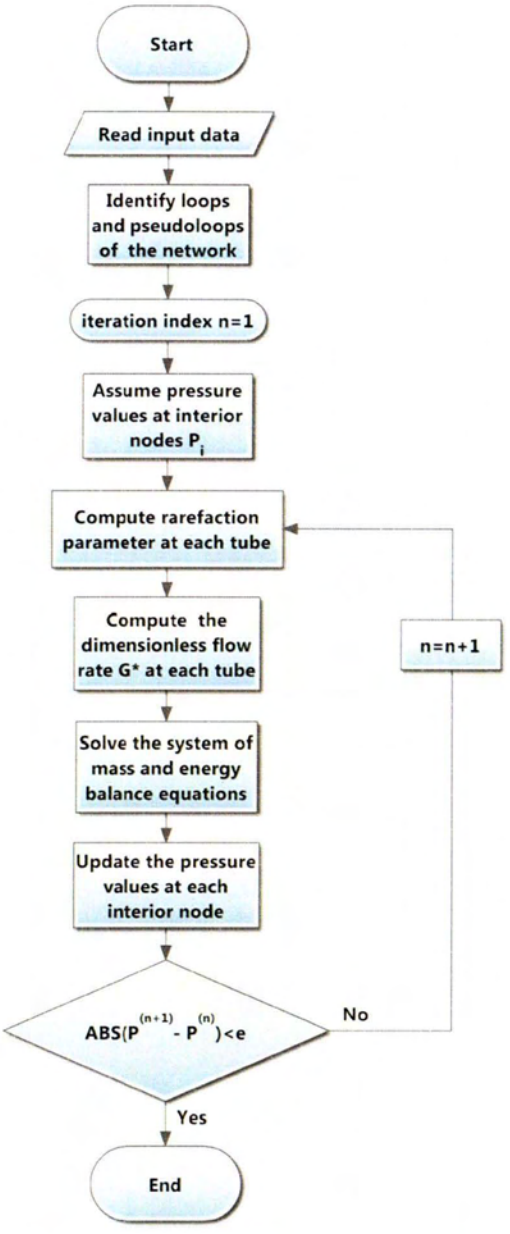

Figure 4: Logic diagram of the integrated steady-state algorithm.

Some pitfalls of the above methodology that may arise are mentioned below for clarity and completeness. If the network geometry given as input is not well defined the algorithm collapses. Some cases that fall in the above category are nodes that have no pipe connection with the rest of the network, pipes that connect a node with itself and wrong numbering of either the nodes or the pipes of the network. Also for the numerical scheme to converge it is mandatory

that a solution of the given network exists. The unconditional convergence of steps 1 to 7 is guaranteed only when node pressures and gas supplies are given as boundary conditions to the network while when node demands are imposed the network solution can be constituted infeasible.

3.5 Time dependent gas distribution systems – Hybrid scheme

In many cases, gas distribution systems operate under transient conditions instead of steady-state. The time dependency of a network can originate from various sources such as non-constant node demand or supply, valve events or tanks with variable pressure. In this study only the latter case is considered. It is clear though that for all of the above cases the time must be discretized and the whole network must be solved at each time step with variable conditions. The above methodology while easy and straightforward in its implementation is computationally demanding for small or medium sized distribution systems and prohibitive for large networks. Thus for complex distribution systems with thousands and nodes and pipes a hybrid model must be applied. To clarify the hybrid coupling it is auxiliary to consider the simple network shown in Fig. 5.

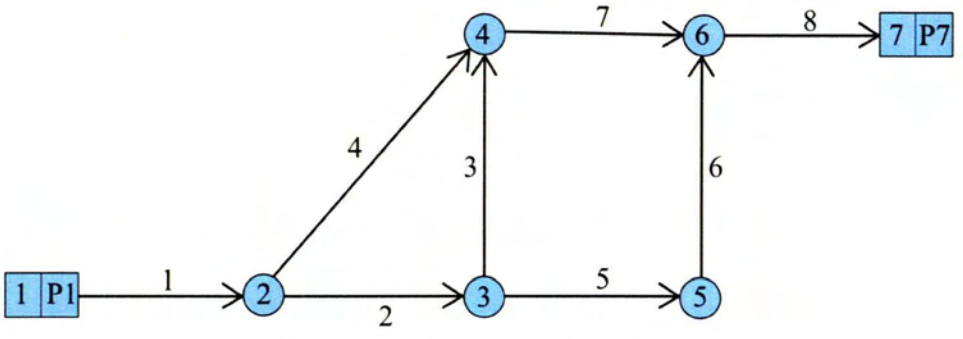

Figure 5: Transient example network.

Assume without the loss of generality that fixed-grade node {1} is a tank of infinite volume while fixed-grade node {7} represents a tank of finite volume V with an initial pressure $P_7 > P_1$. It is observed that gas from node {7} will flow towards node {1} due to the pressure

difference and thus the pressure at node {7} will gradually decrease until the network reaches a steady state. It is also clear that the process in the finite volume chamber and the process of the gas flow through the network are coupled. However, and explicit-type coupling of the two processes as described in [42, 43] can be applied. The time that characterizes the flow inside a tube is defined as the time needed to cross the tube radius with the most probable velocity of the gas and is provided below:

$$t_m = \frac{R}{u_0} \tag{3.5.1}$$

where R is the tube radius and u_0 is the most probable velocity of the conveying gas. While the characteristic time of the reservoir is given as:

$$t_M = \frac{V}{u_0 R^2} \tag{3.5.2}$$

where V is the volume of the reservoir. It is observed that for typical systems $V >> R^3$ and therefore $t_M \gg t_m$. Thus a pressure change inside a reservoir has a quasi-steady response by the flow rates of the network which allows the explicit coupling of the two models. More specifically, it is stated that the hybrid coupling method can be applied when $t_M / t_m \geq 10$. The chamber pressure is assumed to follow the Ideal Gas Law and thus the pressure change can be written as:

$$\frac{dP(t)}{dt} = \frac{\dot{m} R_g T}{V} \tag{3.5.3}$$

where R_g is the conveying gas constant, T is the temperature of the chamber, and $\dot{m}$ is the mass flow inserting or exerting the chamber. In the simple case that the network contains only one finite volume tank, the gas flow $\dot{m}$ can be written as a function of only the chamber's pressure and thus Eq. (3.5.3) is reduced to an ordinary differential equation which can be explicitly solved

with respect to the chamber's pressure $P(t)$. For the mass flow rate $\dot{m}$ the network must be solved for various chamber pressures in order to create a data base. Then, $\dot{m}$ can be interpolated with respect to $P(t)$ and the pressure evolution inside the chamber is easily derived by explicitly integrating equation Eq. (3.5.3). It is clear that once the mass flow rate data base is known the computational effort required to integrate Eq. (3.5.3) is minimal compared to the solution of the fully-coupled problem. However, in the general case where the network contains N finite volume tanks Eq. (3.5.3) must be solved individually for every tank:

$$\frac{dP_i(t)}{dt} = \frac{\dot{m}_i R_g T_i}{V_i} \quad , \quad i = 1, 2...., N \tag{3.5.4}$$

where the mass flow rate inserting or exerting vessel i depends on the pressures of each chamber and must be written as:

$$\dot{m}_i = F\left(P_1, P_2, ..., P_N\right) \quad , \quad i = 1, 2...., N \tag{3.5.5}$$

In order to express each $\dot{m}_i$ the creation of a data base with N dimensions is required. Thus, it is stated that hybrid-coupling although valid for networks with N finite volume vessels, is computationally efficient for up to $N \leq 2$.

3.6 Benchmarking

To verify the code and its accuracy three benchmark problems will be solved two of them being steady-state problems while the remaining one being time-dependent. The first benchmark network which belongs in the slip flow regime (rough vacuum) is shown in Fig. 6. In this gas rarefaction range the Navier Stokes equations subject to slip boundary conditions are still valid and well established hydrodynamic network solvers may be implemented [44]. Thus a comparison between the corresponding results is plausible.

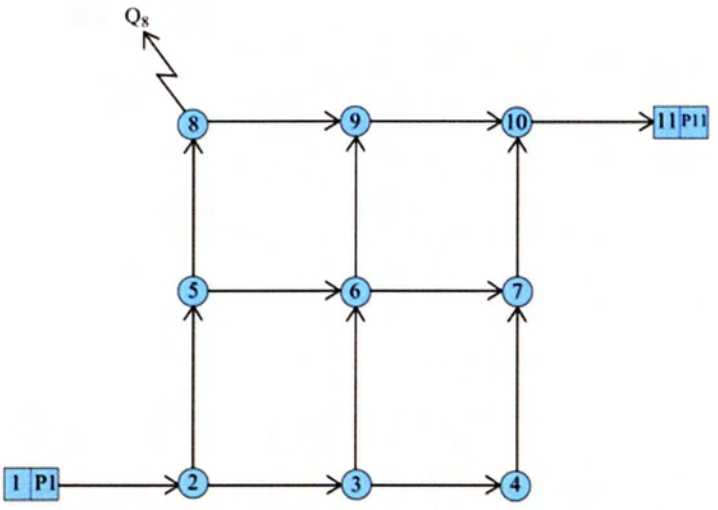

Figure 6: First steady state benchmark network.

The network shown in Fig. 6 consists of 14 tubes, 9 junction nodes {2, 3,... 10} , 2 fixed pressure nodes{1, 11}, 4 loops and 1 pseudoloop. The tubes of the network have various lengths and diameters in the wide range of $2 \leq L/R \leq 1200$ and are tabulated in Table 4. The conveying gas is argon (Ar) at reference temperature T_0= 293.7 K with the following properties: molar mass m = 39.95 g/mole, gas constant R = 208 J/kg/K, viscosity $\mu = 2.280\times10^{-5}$ Pa s. The pressures at nodes 1 and 11 are fixed at 2 Pa and 0.4 Pa respectively. For generality purposes a demand equal to 2×10^{-7} kg/s has been added at node 8. The sample network described above is solved via both the present kinetic network algorithm and a Matlab solver based on the hydrodynamic equations with velocity slip boundary conditions [44]. The comparison of the pipe flow rates and node pressures between the two approaches are provided in Tables 3 and 4. It is clearly observed that there is a very good agreement between the results of the two approaches with the higher deviations being for the pressure 0.65% at node 8 and for the mass flow rates 2.9% at tube 13.

Table 3: Pressure [Pa] at the nodes of the sample network shown in Fig. 6.

Node number	1	2	3	4	5	6	7	8	9	10	11
Kinetic code	2.0	1.418	0.895	0.716	1.337	0.781	0.715	1.107	0.929	0.664	0.400
Hydro-dynamic code	2.0	1.413	0.896	0.718	1.332	0.779	0.716	1.099	0.925	0.661	0.400

Table 4: Tube mass flow rate [Kg/s] of the sample network shown in Fig. 6.

Tube	Nodes	Length L [m]	Diameter D [m]	Average δ_0	Kinetic mass flow rate [Kg/s]	Hydrodynamic mas flow rate [Kg/s]
1	1 – 2	20	0.20	21.4	1.66×10^{-6}	1.67×10^{-6}
2	2 – 3	5	0.10	7.25	3.35×10^{-7}	3.33×10^{-7}
3	3 – 4	6	0.15	7.58	3.30×10^{-7}	3.28×10^{-7}
4	2 – 5	100	0.50	43.2	1.33×10^{-6}	1.34×10^{-6}
5	3 – 6	60	0.10	5.26	5.14×10^{-9}	5.04×10^{-9}
6	4 – 7	0.4	0.40	18.0	3.30×10^{-7}	3.28×10^{-7}
7	5 – 6	20	0.10	6.65	8.55×10^{-8}	8.37×10^{-8}
8	6 – 7	2	0.20	9.39	9.38×10^{-7}	9.53×10^{-7}
9	5 – 8	8	0.20	15.3	1.24×10^{-6}	1.26×10^{-6}
10	6 – 9	80	0.40	21.5	-8.48×10^{-7}	-8.65×10^{-7}
11	7 – 10	2.5	0.25	10.8	1.27×10^{-6}	1.28×10^{-6}
12	8 – 9	30	0.30	19.2	1.04×10^{-6}	1.06×10^{-6}
13	9 – 10	15	0.15	7.49	1.96×10^{-7}	1.90×10^{-7}
14	10 – 11	1.5	0.15	5.01	1.46×10^{-6}	1.47×10^{-6}

The second benchmark network belongs in the slip regime and is shown in Fig. 7. The above network consists of 24 tubes, 20 junction nodes, 4 fixed pressure nodes, 5 loops and 3 pseudoloops. The tubes of the network have various lengths and diameters in the range of $10 \leq L/R \leq 300$. The conveying gas is air at reference temperature $T_0 = 293.7$ K with the following properties: molar mass m = 28.319 g/mole, gas constant R = 286.9 J/kg/K, viscosity $\mu = 1.837 \times 10^{-5}$ Pa s. The pressure at node 1 is fixed at 1 Pa while the pressure at nodes 15, 18, 20 is set to 10 Pa. Also at nodes 7 and 8 a demand of to 1×10^{-6} kg/s has been added. The comparison between the two approaches for the pipe mass flow rates as well as for the node pressures is provided in Tables 5 and 6. It is observed that the higher deviations of the two approaches are 0.16% for the pressures at node 6 and 1.9% for the mass flow rates at tube 18. The good agreement between the two approaches is justified by the rarefaction regime of the network, as well as the L/R range of the pipes.

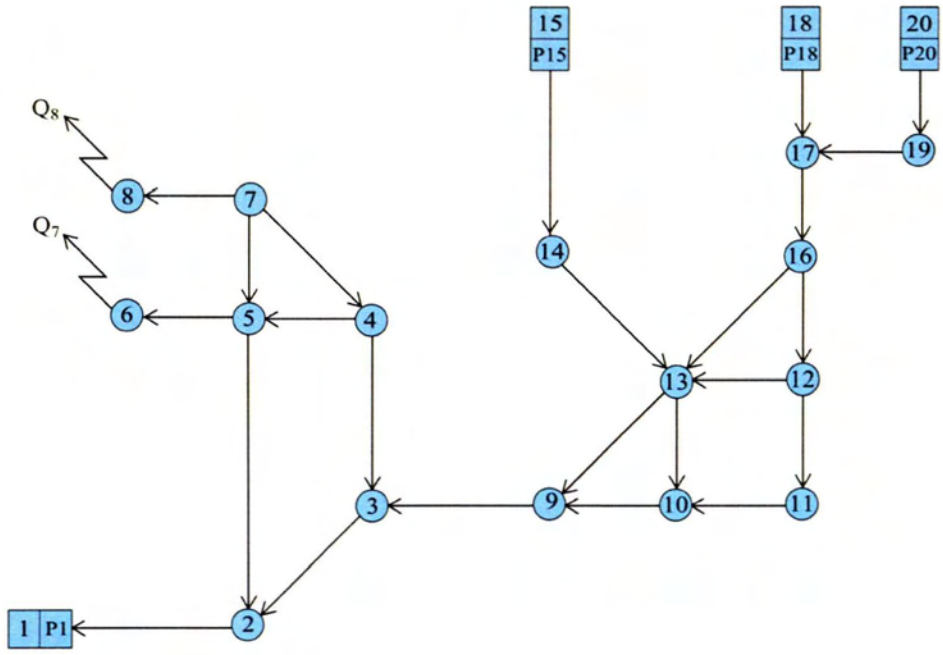

Figure 7: Second steady state benchmark network.

Table 5: Tube mass flow rate [Kg/s] of the sample network shown in Fig. 7.

Tube	Nodes	Length L [m]	Diameter D [m]	Average δ_0	Kinetic mass flow rate [Kg/s]	Hydrodynamic mas flow rate [Kg/s]
1	2 – 1	10	0.50	53.17	2.00×10^{-04}	2.00×10^{-04}
2	3 – 2	15	0.20	67.33	5.18×10^{-05}	5.19×10^{-05}
3	4 – 3	12	0.50	259.6	-1.50×10^{-04}	-1.51×10^{-04}
4	5 – 2	2.5	0.50	76.08	1.48×10^{-04}	1.49×10^{-04}
5	4 – 5	18	0.25	83.67	9.62×10^{-05}	9.66×10^{-05}
6	5 – 6	4	0.40	63.14	1.00×10^{-06}	1.00×10^{-06}
7	7 – 4	12	0.20	72.81	-5.39×10^{-05}	-5.39×10^{-05}
8	7 – 5	20	0.40	74.94	5.29×10^{-05}	5.29×10^{-05}
9	7 – 8	20	0.50	108.3	1.00×10^{-06}	1.00×10^{-06}
10	9 – 3	8	0.40	217.3	2.02×10^{-04}	2.02×10^{-04}
11	10 – 9	10	0.20	115.0	1.03×10^{-05}	1.04×10^{-05}
12	13 – 9	10	0.40	231.1	1.92×10^{-04}	1.92×10^{-04}
13	13 – 10	5	0.25	148.3	9.75×10^{-06}	9.89×10^{-06}
14	14 – 13	15	0.10	62.95	1.08×10^{-06}	1.08×10^{-06}
15	15 – 14	4	0.50	331.6	1.08×10^{-06}	1.08×10^{-06}
16	11 – 10	10	0.50	295.1	5.53×10^{-07}	5.52×10^{-07}
17	12 – 11	14	0.20	118.3	5.53×10^{-07}	5.52×10^{-07}
18	12 – 13	15	0.10	59.42	-5.50×10^{-08}	-5.61×10^{-08}
19	16 – 13	12	0.50	302.5	2.00×10^{-04}	2.01×10^{-04}
20	16 – 12	10	0.10	60.31	4.98×10^{-07}	4.96×10^{-07}
21	17 – 16	30	0.50	317.5	2.01×10^{-04}	2.01×10^{-04}
22	18 – 17	5	0.50	329.8	1.99×10^{-04}	1.99×10^{-04}
23	19 – 17	15	0.25	164.4	1.91×10^{-06}	1.94×10^{-06}
24	20 – 19	20	0.25	165.3	1.91×10^{-06}	1.94×10^{-06}

Table 6: Pressure [Pa] at the nodes of the sample network shown in Fig. 7.

Node number	Kinetic Code	Hydrodynamic code	Node number	Kinetic Code	Hydrodynamic code
1	1.000	1.000	11	8.899	8.891
2	2.207	2.210	12	8.932	8.924
3	7.946	7.937	13	8.987	8.980
4	7.711	7.701	14	10.00	10.00
5	2.382	2.386	15	10.00	10.00
6	2.378	2.382	16	9.257	9.251
7	3.268	3.264	17	9.893	9.892
8	3.262	3.260	18	10.00	10.00
9	8.439	8.430	19	9.939	9.939
10	8.898	8.890	20	10.00	10.00

The network shown in Fig. 7 is now simulated as a time dependent problem in order to benchmark the hybrid integration code. All the operational data described above hold (geometry, fixed pressures, demands, conveying gas) with the exception of nodes 15,18 and 20 which are now connected to a reservoir with a volume of 50 m^3. Thus the initial pressure of 10 Pa will change according to the mass balance of the reservoir until a steady-state has been reached. The network described above is tackled both with the hybrid integration code and by directly solving the full time-dependent problem with the kinetic code. For the hybrid integration the steady state kinetic algorithm is used to create a data base between the pressure of the reservoir and the mass flow rate exiting the reservoir and then the integration of the reservoir's mass balance equation is performed as described in chapter 3.5. For the simulation of the full time-dependent a network has to be solved in which the pressure of the reservoir at nodes 15,18 and 20 is defined by the ideal gas law in each time step. The advantage of the fully coupled problem is that all the pressures and mass flow rates of the network are provided for each time step while the hybrid simulation only provides the finite volume tank pressure. In Figs. 8 and 9 the pressure of specific nodes and the mass flow of certain tubes over 200 s is presented. It is observed that for the indicative nodes presented, the pressures decrease monotonically and show a similar qualitative behavior. The same behavior is observed for the mass flow rates in Fig. 9.

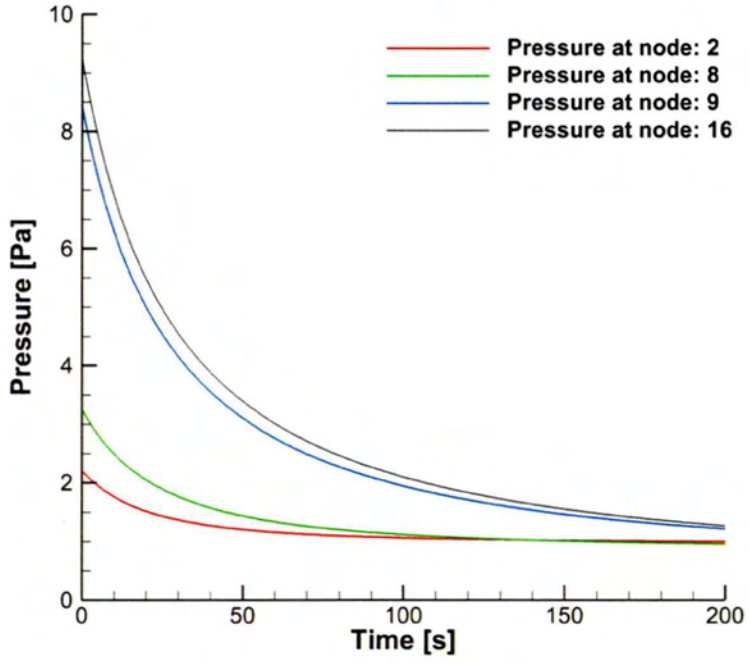

Figure 8: Pressure evolution for nodes 2, 8, 9 and 16 of the gas network shown in Fig. 7.

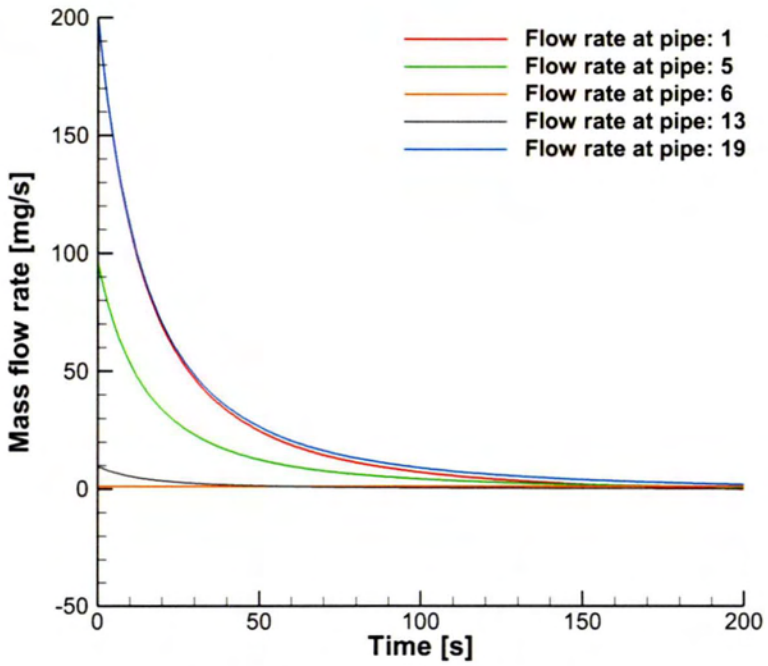

Figure 9: Mass flow rate evolution for pipes 1, 5, 6, 13 and 19 of the gas network shown in Fig. 7.

The pressure evolution of the tank with respect to time is shown in Fig. 10 for both approaches. A perfect agreement is observed between the hybrid-coupling method and the direct simulation of the full time dependent network as the higher deviation over the course of 1000 s is below 0.02%. The CPU used for both simulations was an Intel i5-6200U at 2.3 GHz and the computational time required for the direct transient simulations was 231.2 s while only 0.8 s for the hybrid coupling.

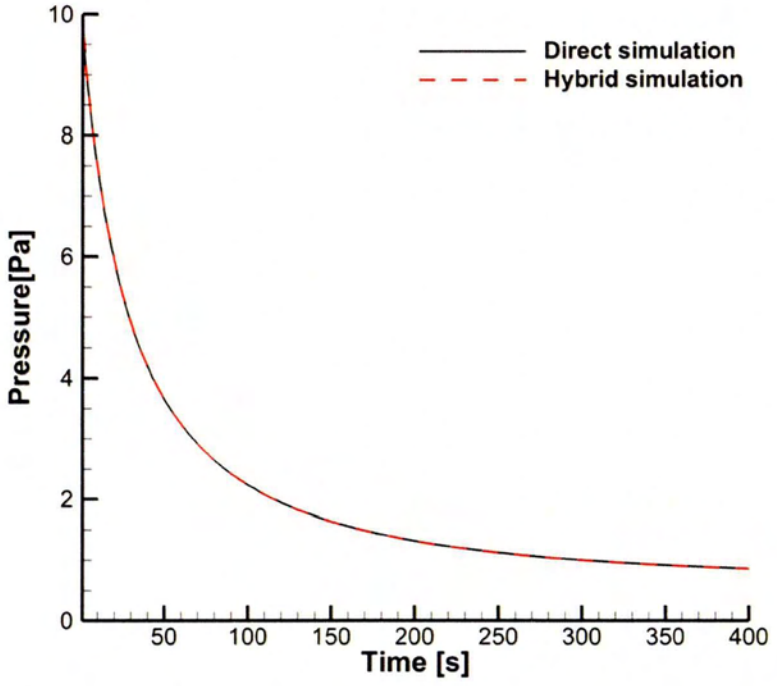

Figure 10: Comparison of pressure evolution inside the finite volume tank with the direct and hybrid schemes.

Chapter 4: The ITER primary vacuum pumping system

4.1 Geometry

The successful operation of ITER requires the largest and more complex vacuum systems yet to be built. The vacuum spaces comprise the main tokamak, the cryostat vacuum for thermal insulation of the superconducting coils, four neutral beam injectors and auxiliary vacuum for diagnostic, radio frequency heating systems and cryogenic circuits. The ITER tokamak will be fuelled with equimolar DT and will require neutralized gas in the divertor to be pumped out in order to balance the fuelling and remove the fusion helium and other impurities in the exhaust. The initial ITER design has undergone continuous revisions in order to reduce costs and solve engineering issues associated with its performance.

The most recent geometric configuration of the ITER divertor is visualized in the 2012 CATIA drawings of the ITER divertor section, which provide detailed geometrical data of the divertor ring with the 54 cassettes and interconnecting paths as well as of the pumping ducts and ports. These drawings have been used within the ITER Physics activities of the 2012-13 European Fusion Development Agreement (EFDA) program to simulate the neutral gas flow in the divertor pumping system. Following the 2012 drawings and the associated reports [45-47] as well as the recently published work [48], the divertor pumping system has been approximated by the pipe network shown in Figs. 11 and 12. All cassettes are considered identical to each other and are sequentially numbered (1-54).

Fig. 11 shows a view of the cross section along a cassette connected to a pump and the corresponding pipe network approximating the geometry of the actual gas flow path along the cassette cross section. The regions of the dome, the inner and outer divertor arm gaps as well as the inlet and the outlet slots are indicated. The channel flow configurations of the upper and lower parts of the cassette are approximated by 25 and 16 channels respectively of various lengths and diameters. The upper part consists of nodes 1 to 26 and the lower part of nodes 27 to 43. They are interconnected with 2 pipes resulting to a total of 43 channels and 43 nodes per cassette. The 6 nodes {1, 10, 14, 18, 26, 43} with given pressure (fixed grade nodes) are specified. Through these nodes the pipe network representing the flow along a cassette is open to the plasma side. Six out of the 54 cassettes, and more specifically cassettes 11, 17, 29,35, 47 and

53, are connected to the six cryopumps located at ports 4, 6, 10, 12, 16 and 18 respectively [47]. The pumping duct nodes connecting each of the six cassettes to the corresponding pump are shown for a typical case in Fig. 11. Finally, the 11 nodes {6, 9, 13, 17, 21, 28, 31, 33, 35, 38, 40} connecting this cassette to its adjacent cassette in the toroidal direction, defined as toroidal connection nodes, are also presented in Fig. 11. The pipe network simulating the geometry of the actual gas flow path between adjacent cassettes in the toroidal direction along the divertor ring, as well as through the gaps between the cassettes facing the plasma side on a plane normal to the toroidal direction is shown in Fig. 12.

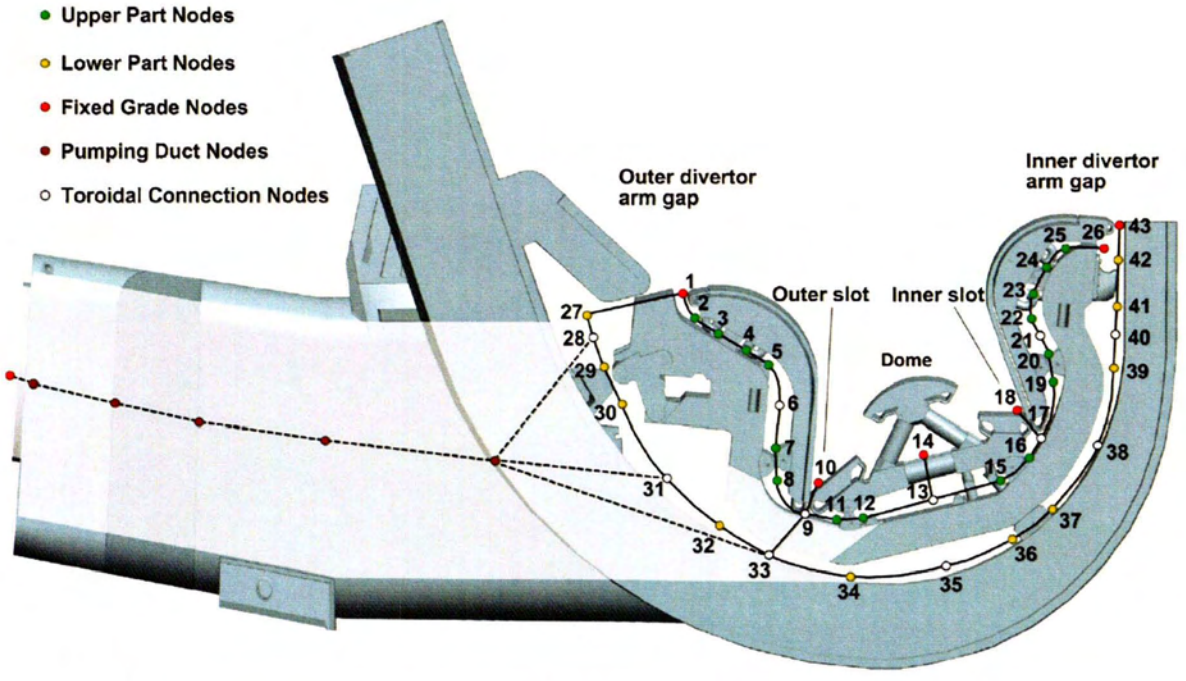

Figure 11: View of the cross section along a cassette connected to a pump and schematic representation of the corresponding pipe network approximating the geometry of the actual gas flow path.

According to the 2012 drawings the distance between adjacent cassettes is 20 mm. The 11 connection pipes between two cassettes (5 for the upper part and 6 for the lower part) originated from the corresponding toroidal connection nodes, mentioned in the description of Fig. 11, are shown and create the segment of the pipe network representing the gas flow in the toroidal direction. In addition, the middle points of these 11 pipes are interconnected, as

demonstrated in Fig. 12, in order to produce the segment of the pipe network representing the geometry of the gas flow through the gap openings between the cassettes which is open to the plasma side. It consists from 19 channels defined by the so-called 15 gap nodes including the 4 fixed grade nodes {45, 48, 53, 56} where the pressure is given, all shown in Fig. 12. Thus, the pipe network in Fig. 12 consists of $2 \times 11 + 19 = 41$ channels.

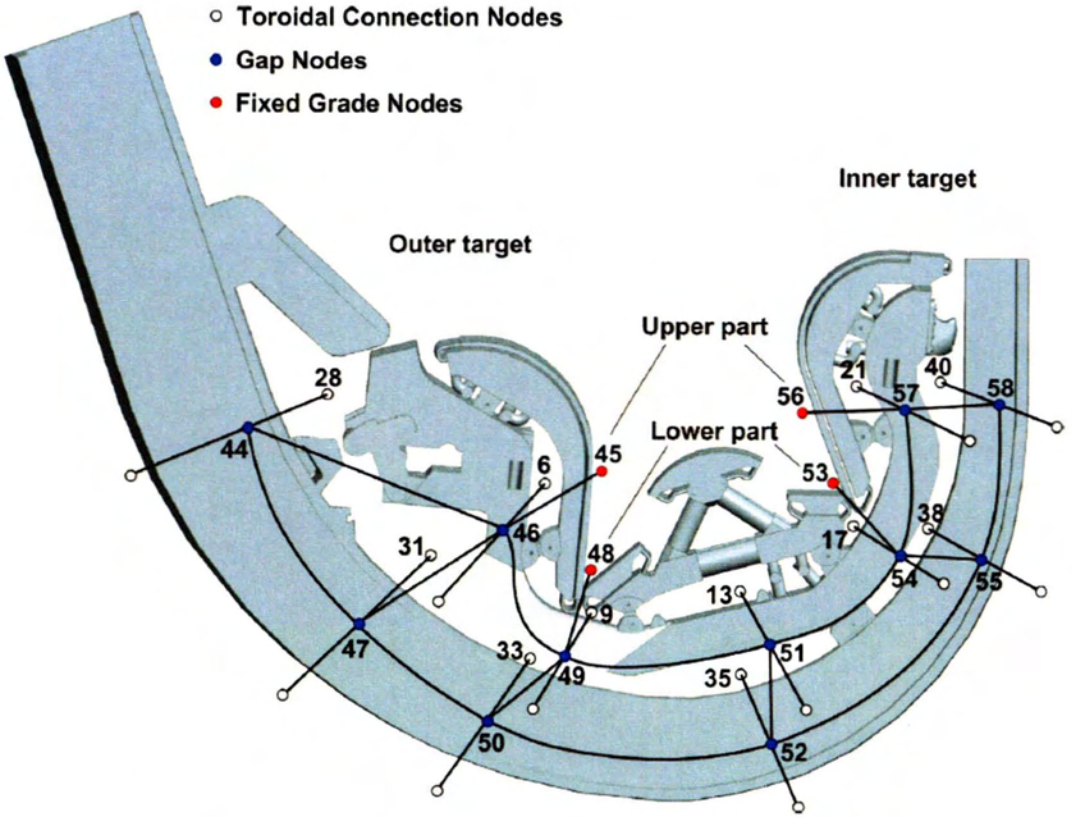

Figure 12: Schematic representation of the pipe network approximating the geometry of the actual gas flow between adjacent cassettes in the toroidal direction along the divertor ring and through the gaps between the cassettes facing the plasma side.

The whole pipe network for the ITER divertor pumping system consists of the 43 + 41 = 84 channels per cassette times 54 cassettes plus 8 channels per pump times 6 pumps resulting to a total of 4584 pipes. The total number of nodes is 3168. At each cassette with the associated gap there are a total of 10 fixed grade nodes (indicated in Figs. 11 and 12). Thus the total number of

fixed pressure nodes is equal to 540 plus the 6 fixed grade nodes at the inlet of the pumps. The total number of loops and pseudoloops are 1417 loops and 545 respectively.

In order to convert a pipe of arbitrary cross section to its respective circular one the concept of the equivalent diameter has been applied in this study. The exact measurements of all the piping elements lengths and diameters are provided in Table 7.

Table 5: Node numbers, length and diameter of all piping elements shown in Figs. 11 and 12.

Pipe nodes	Length [m]	Diameter [m]	Pipe nodes	Length [m]	Diameter [m]	Pipe nodes	Length [m]	Diameter [m]
1 - 2	0.251	0.310	28 - 29	0.192	0.714	47 - 89	0.010	0.998
2 - 3	0.186	0.266	29 - 30	0.356	0.380	33 - 50	0.010	0.533
3 - 4	0.121	0.073	30 - 31	0.534	0.622	50 - 91	0.010	0.533
4 - 5	0.186	0.257	31 - 32	0.534	0.622	35 - 52	0.010	0.668
5 - 6	0.269	0.352	32 - 33	0.469	0.283	52 - 93	0.010	0.668
6 - 7	0.269	0.352	33 - 34	0.469	0.283	38 - 55	0.010	0.624
7 - 8	0.169	0.108	34 - 35	0.568	0.352	55 - 96	0.010	0.624
8 - 9	0.379	0.290	35 - 36	0.568	0.352	40 - 58	0.010	0.539
9 - 10	0.073	0.151	36 - 37	0.250	0.197	58 - 98	0.010	0.539
9 - 11	0.230	0.475	37 - 38	0.624	0.248	45 - 46	0.210	0.159
9 - 33	0.379	0.290	38 - 39	0.624	0.248	48 - 49	0.196	0.128
11 - 12	0.145	0.183	39 - 40	0.161	0.372	53 - 54	0.196	0.129
12 - 13	0.545	0.348	40 - 41	0.161	0.372	56 - 57	0.192	0.157
13 - 14	0.279	0.445	41 - 42	0.300	0.133	46 - 44	0.135	0.156
13 - 15	0.545	0.346	42 - 43	0.250	0.333	46 - 47	0.668	0.160
15 - 16	0.197	0.103	6 - 46	0.010	0.891	49 - 50	0.329	0.145
16 - 17	0.304	0.217	46 - 64	0.010	0.891	51 - 52	0.379	0.180
17 - 18	0.104	0.140	9 - 49	0.010	0.606	54 - 55	0.315	0.149
17 - 19	0.304	0.217	49 - 67	0.010	0.606	57 - 58	0.383	0.157
19 - 20	0.183	0.120	13 - 51	0.010	0.828	46 - 49	0.750	0.106
20 - 21	0.142	0.329	51 - 71	0.010	0.828	49 - 51	0.107	0.106
21 - 22	0.142	0.329	17 - 54	0.010	0.626	51 - 54	0.105	0.106
22 - 23	0.149	0.251	54 - 75	0.010	0.626	54 - 57	0.629	0.099
23 - 24	0.116	0.075	21 - 57	0.010	0.813	44 - 47	0.108	0.143
24 - 25	0.147	0.214	57 - 79	0.010	0.813	47 - 50	0.100	0.119
25 - 26	0.239	0.156	28 - 44	0.010	0.667	50 - 52	0.104	0.082
1 - 27	0.559	0.239	44 - 86	0.010	0.667	52 - 55	0.144	0.080
27 - 28	0.192	0.714	31 - 47	0.010	0.998	55 - 58	0.785	0.099

4.2 Results of the ITER divertor primary pumping system

Simulations have been performed to model the burn and dwell phases for various divertor dome pressures. The input parameters are the ones prescribed in [48]. They have been obtained from the B2-EIRENE code modeling an ITER scenario where the plasma consists mainly from deuterium with the ratio of the fusion over the input power to be equal to Q_{DT}= 10 and the power entering the scrape-off layer equal to 100 MW. These input parameters have been also used in [49]. Following [48], three different pressure scenarios at the burn phase corresponding to total pressures of 2.6 Pa, 4.1 Pa and 9.9 Pa are simulated. They are related to low, medium and high dome pressure scenarios. Since only the dominant deuterium gas fraction is considered the resulting partial pressures at the 10 fixed grade nodes are given in Table 8 and they are the same with the data of Table 1 in [48].

Table 6: Partial pressure [Pa] of deuterium (D2) at fixed pressure nodes for the three operating scenarios in the burn phase [48].

Node number	Corresponding location in [48]	Low-p	Mid-p	High-p
1	E	8.2×10^{-4}	1.0×10^{-3}	8.1×10^{-4}
10	D	3.65	7.20	15.0
14	C	1.85	3.10	7.82
18	B	10.4	12.5	23.6
26	A	6.7×10^{-5}	2.6×10^{-4}	8.8×10^{-4}
43	A	6.7×10^{-5}	2.6×10^{-4}	8.8×10^{-4}
45	Upper part of gap, outer target	0.20	0.30	0.30
48	Lower part of gap, outer target	8.30	18.5	33.7
53	Lower part of gap, inner target	32.3	42.7	70.1
56	Upper part of gap, inner target	0.08	0.20	0.60

The same pressures are given to the fixed grade nodes in all 54 cassettes and the associated gaps between the cassettes. The operating temperature is set at 420 K and the conveying gas is deuterium (D2) with molecular mass m = 4.0282 g/mole, gas constant Rg= 2064.1 J/kg/K, and viscosity μ= 1.590×10^{-5} Pa s. The limiting pumping speed of the cryopumps, has been taken into consideration and for D2 was set equal to 55 m^3/s. Thus,

simulations have been performed in an iterative manner to meet this requirement. More specifically, initially a low pressure is given at the inlet of each cryopump, resulting to a pumping speed much larger than the limiting value. Then, each pump pressure is increased gradually until the resulting throughput and inlet pump pressure correspond to the prescribed pumping speed limit. Based on these data the local gas rarefaction in the network varies in a wide range of the Knudsen number from the free molecular limit through the transition up to the slip regime.

4.2.1 Burn Phase

The configuration described above is implemented to simulate the three-dimensional gas flow pattern in the 2012 ITER divertor primary pumping system. For the input data of Table 8 qualitative results are provided, including the produced gas flow patterns in each cassette as well as in the open gaps between adjacent cassettes and along the divertor ring.

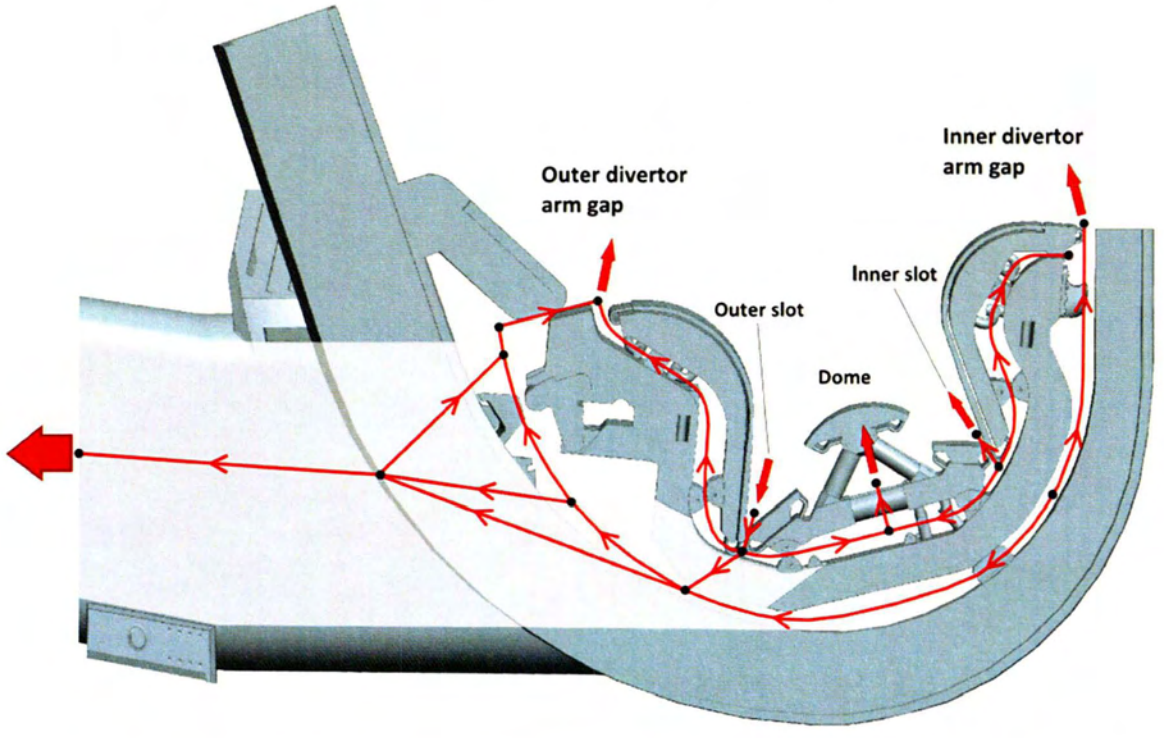

Figure 13: Direction of the gas flow in the pipe network simulating the actual gas flow path in the cross section along a cassette connected to a pump in the burn phase.

In Fig. 13 the gas flow path in a cross section along a cassette, as described in Fig. 11, is shown. This flow pattern is qualitatively the same in all three pressure scenarios investigated in the burn phase and applies to all 54 cassettes. The gas enters from the plasma chamber into each cassette via the outer slot fixed grade node 10. One part of the gas remains in the upper part of the cassette and flows in opposite directions returning finally back into the plasma from the fixed grade nodes at the dome, the inner slot and also the inner and outer divertor arm, defined by the nodes 14, 18, 26 and 1 respectively. Another part of the gas reaches the lower part of the cassette and then is separated with one fraction flowing toward vacuum pump and the remaining one returning to the plasma via the outer and inner divertor arm gap nodes 1 and 43 respectively. Also strong recirculation is observed behind the outer divertor arm gap with the gas pumped from nodes 31 and 33 finally escaping back to the plasma through node 1.

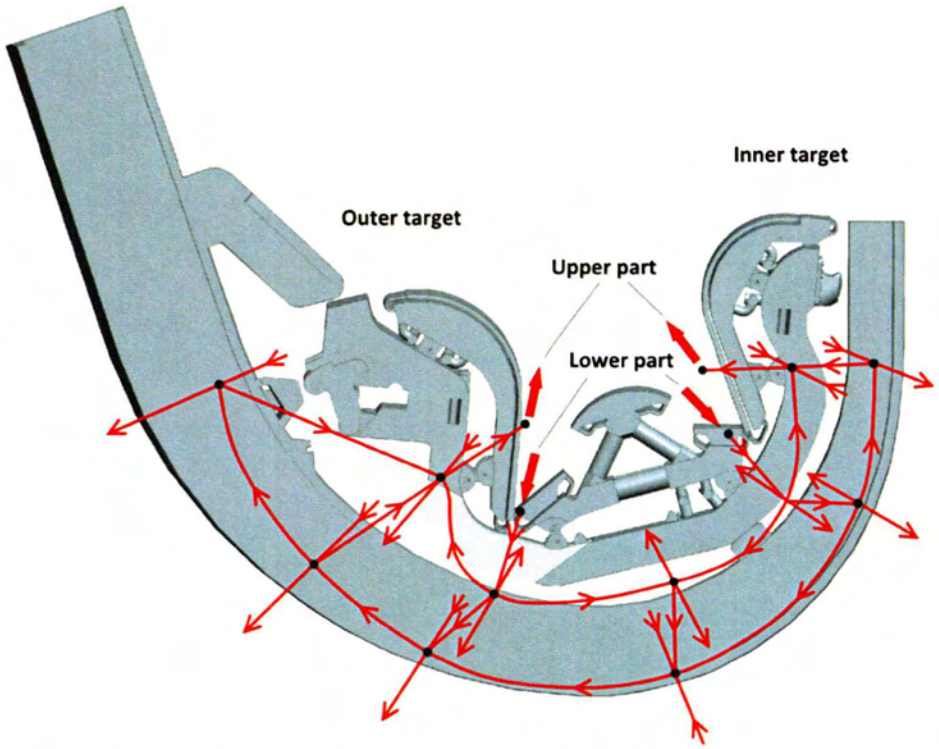

Figure 14: Direction of the gas flow in the pipe network simulating the actual gas flow path between adjacent cassettes in the toroidal direction along the divertor ring and through the gaps between the cassettes facing the plasma side in the burn phase.

In Fig. 14 the gas flow path along the divertor ring and in the open gaps between adjacent cassettes, as described in Fig. 12, is shown. It is clearly seen that gas is entering the gap network from the high pressure fixed grade nodes 48 and 53 in the lower part and is returning back to the plasma from the low pressure fixed grade nodes 45 and 56 in the upper part. This recirculation flow pattern is the same in all 54 cassettes. The gas which remains in the gap network flows toward the inner or outer targets and then it is conveyed to the adjacent cassettes via the 11 interconnecting channels in the toroidal direction. The flow along the divertor ring via the toroidal connections is quite complex and differs depending on the location of the toroidal interconnecting channel (if it is in the inner or outer part of the gap) as well as on the cassette position with regard to the pumping ports. However, it is clear that the bulk of the gas being pumped out is conveyed along the divertor ring through the toroidal connections located at nodes 31 and 33 at the lower part of the cassettes while gas is recirculating through most of the remaining toroidal connections to finally flow back to the plasma chamber.

A detailed quantitative description of the gas flow configuration in terms of the deduced throughputs is now provided. In Figs. 15 and 16 the computed throughputs in the burn phase toward the pumps and the plasma respectively are plotted in terms of the dome pressure with four pumps running. The operating pumps are the ones located at pumping ports 4, 6, 10 and 12. Due to the great uncertainty of the gap network modeling a sensitivity analysis of the results is also provided. In this sensitivity analysis two extra scenarios are investigated. At first the gap width is set to 10 mm and then no gap between cassettes is assumed. The results of these two scenarios are also provided in Figs. 15 and 16. As expected in all the cases as the dome pressure increases the throughputs are also increased monotonically. Also, as the gap size is decreased both throughputs toward the pumps and the plasma are decreased. Furthermore, comparing between the throughputs in Fig. 15, it is noted that when the gap width is reduced from 20 mm to 10 mm the pump throughput is reduced in the low, medium and high pressure dome scenarios about 20%, 19% and 12%. While the corresponding reductions in Fig. 16 for the throughputs toward the plasma are 53%, 51% and 42%. Thus, it is stated that the area of the gap between the cassettes affects more drastically the flow toward the plasma rather than the flow toward the pumps. This remark is also supported by the throughput reductions in the limiting no gap scenario, where the reductions are much higher. By taking the ratios of the corresponding throughputs toward the pumps and the plasma plotted in Figs. 15 and 16 it is deduced that for the

20 mm gap width and the low pressure scenario only 6% of the incoming throughput is pumped, while the remaining 94% is returning to the plasma chamber. As the dome pressure is increased the ratios of the pumped gas is slightly increased. It is also increased as the gap size is reduced becoming about 10% for the 10 mm gap and 13% for the no gap case.

In addition, in Figs. 15 and 16 a comparison with the throughputs reported in [48] for the 20 mm gap width is performed. The relative error between the computed throughputs in [48] and the present ones is 4 – 22% in the flow toward the pumps and 32 – 50% in the flow toward the plasma. In both cases it is seen that the comparison improves as the dome pressure increases. Taking into account the complexity and the different geometrical interpretations of the simulated network and also, the introduced theoretical approximations, the observed discrepancies between the two approaches are reasonable and the overall agreement in the results in the burn phase is considered as very satisfactory.

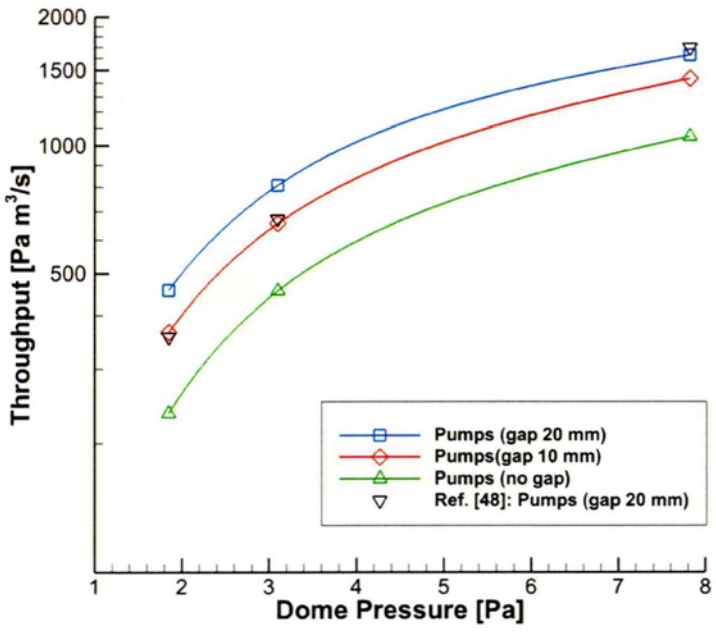

Figure 15: Computed throughputs toward the pumps in the burn phase versus dome pressure with 4 pumps running and various gap widths; corresponding results in [48] are also included.

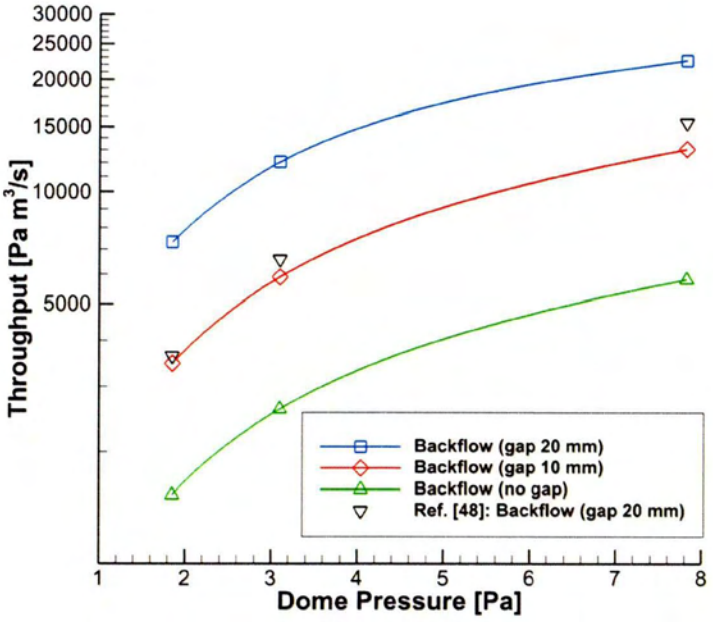

Figure 16: Computed throughputs toward the plasma in the burn phase versus dome pressure with 4 pumps running and various gap widths; corresponding results in [48] are also included.

The computational investigation on the sensitivity of the results in terms of the prescribed geometrical data, which has been performed in Figs. 15 and 16 with regard to the size of the inter-cassette gap, is continued with regard to the pipe radii in the network. More specifically, the importance of the radius size of all pipes in the toroidal direction interconnecting the 54 cassettes is investigated. Simulations have been performed by reducing the radii of all toroidal connections by 20% compared to the ones which have been used in Figs. 15 and 16 with the 20 mm gap width. It has been observed that this radius reduction has a small effect on the throughputs in all three dome pressures. In particular for all dome pressures the pump throughput is slightly reduced (less than 3%), while the corresponding plasma throughput is marginally increased (less than 1%). The fact that the pump throughput is reduced is expected due to the higher pressure drop in the toroidal direction obstructing the gas to be conveyed along the divertor ring in order to be pumped out, which yields a small increase in the backflow of the gas. The importance of the radius size of all pipes in the cross section along a cassette for all 54 cassettes is also investigated. Simulations have been performed by modifying the radii of all pipes of the cassette network by ±20% compared to the ones which have been used in Figs. 15 and 16 with the 20 mm

gap width. It has been found that when the radius of all pipes is reduced by 20% the throughput toward the pumps is increased about 5%, while the backflow throughput is decreased about 7%. The situation is reversed in the 20% radius increase, where the pump throughput is decreased about 8% and the backflow throughput is increased about 10%.These results are on an average basis for all three dome pressures with the corresponding results for each pressure scenario to be close to the average values. More detailed results of the sensitivity analysis both in the toroidal and cassette networks are provided in Table 9. Based on the above sensitivity analysis it is stated that the pipe network output is not strongly affected by varying the radii of the pipes of the network (along a cassette or between cassettes). Furthermore, it may be concluded that the error which may be introduced due to the substitution of the ITER noncircular channels with equivalent circular ones, certainly has no qualitative effect on the resulting flow patterns and affects weakly the resulting pump and plasma throughputs. On the contrary, as it has been seen before, the size of the area of the inter-cassette gaps facing the plasma is of major importance and therefore it must be estimated carefully and accurately.

Table 7: Throughputs [Pa m3 s-1] for the three sensitivity analysis scenarios

Pressure scenario	Reference scenario (20mm gap)	Toroidal radii reduction (20%)	Cassette radii reduction (20%)	Cassette radii increase (20%)
		To Pumps		
Low-p	457.4	445.2	491.5	417.9
Mid-p	808.5	788.5	866.2	740.6
High-p	1629.4	1593.6	1694.9	1537.3
		To Plasma		
Low-p	7324.1	7324.7	6969.7	7832.9
Mid-p	12066.9	12073.1	11140.9	13204.8
High-p	22702.8	22711.6	21026.8	25784.8

In Fig. 17, the case of all six pumps running simultaneously in the burn phase operating mode results is shown. The four pump results are also included. Both throughputs toward the pumps and the plasma versus the dome pressure are plotted. It is seen that with all six pumps running the flow toward the pumps is increased about 50% independent of the dome pressure. On the contrary the flow toward the plasma is slightly decreased by less than 2%. These results are for the 20 mm gap width but all remarks are also valid for the other two gap cases.

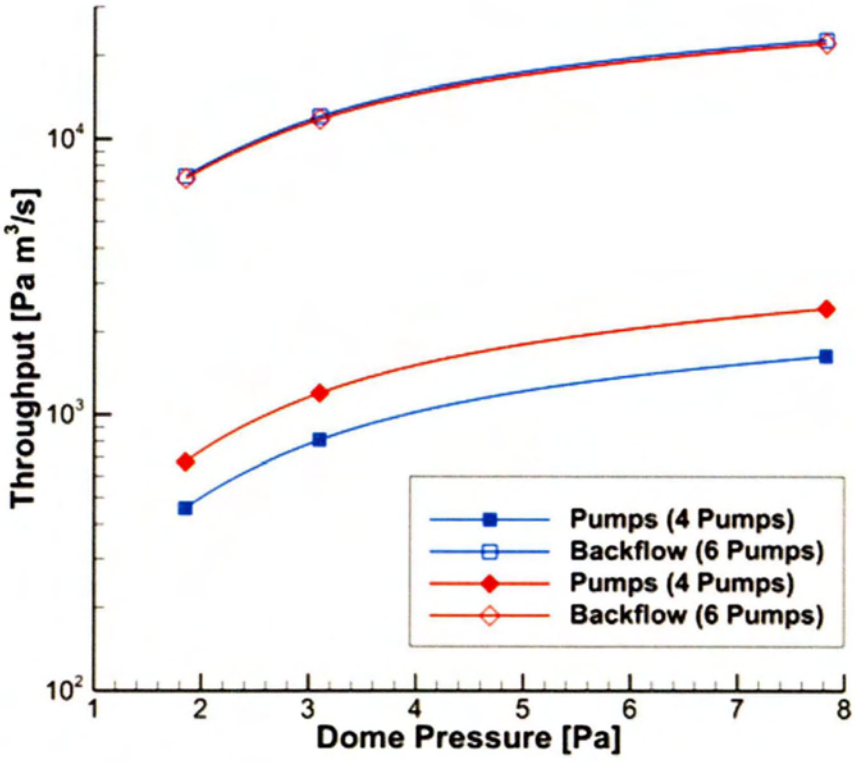

Figure 17: Computed throughputs toward the pumps and the plasma in the burn phase versus dome pressure with 4 and 6 pumps running.

As described in [50] the regeneration process of each cryopump demands 600 s and is divided into four parts: cryogen cold mass recovery, cryo-panel warm up, evacuation and cryo-panel re-cool. Thus for the demanding 3000 s non-inductive burn phase scenario the six cryopumps are envisaged to operate under a pumping sequence in which four of the cryopumps are running and two of them are in regeneration. For this operating scenario the present ITER gas distribution network is simulated using both the low and high pressure data of Table 8. The computed throughputs for each operating pump and the resulting total throughput are given in Tables 10 and 11. It is noted that in all six operational sequences the total throughput is very close to each other and in each operational sequence all individual pump throughputs are well balanced. All these are in favor of moving smoothly from one operating sequence to the next.

Table 8: Throughputs [Pa m3 s-1] for various operating pump sequences for the 3000s non-inductive scenario in the low dome pressure (R denotes regeneration).

Pump port	Pumping sequence					
	1	2	3	4	5	6
18	114.6	114.9	114.0	117.2	R	R
4	R	R	116.9	117.2	114.9	114.9
6	118.2	117.2	R	R	113.7	114.9
10	R	117.2	118.2	114.9	113.7	R
12	116.9	R	R	114.9	114.9	117.2
16	114.0	114.9	114.6	R	R	117.2
Total	463.7	464.2	463.7	464.2	457.2	464.2

Table 9: Throughputs [Pa m3 s-1] for various operating pump sequences for the 3000s non-inductive scenario in the high dome pressure (R denotes regeneration).

Pump port	Pumping sequence					
	1	2	3	4	5	6
18	407.9	408.6	406.5	414.5	R	R
4	R	R	413.9	414.5	408.7	408.6
6	416.6	414.5	R	R	405.9	408.6
10	R	414.5	416.6	408.6	405.9	R
12	413.9	R	R	408.6	408.7	414.5
16	406.5	408.6	407.9	R	R	414.5
Total	1644.9	1646.2	1644.9	1646.2	1629.2	1646.2

4.2.2 Dwell Phase

In the dwell phase the vacuum vessel needs to be pumped down to the base pressure between the 400 s burn of successive plasma pulses. After the plasma pulses the exhaust gases which are enclosed in the vacuum vessel are at rest and thus a constant pressure is assumed inside the vacuum chamber. This pressure is then given as the boundary condition to all the fixed grade nodes facing the vessel in order to simulate the dwell phase. For the input data described above again both qualitative results are provided, including the produced gas flow patterns in each cassette as well as in the open gaps between adjacent cassettes.

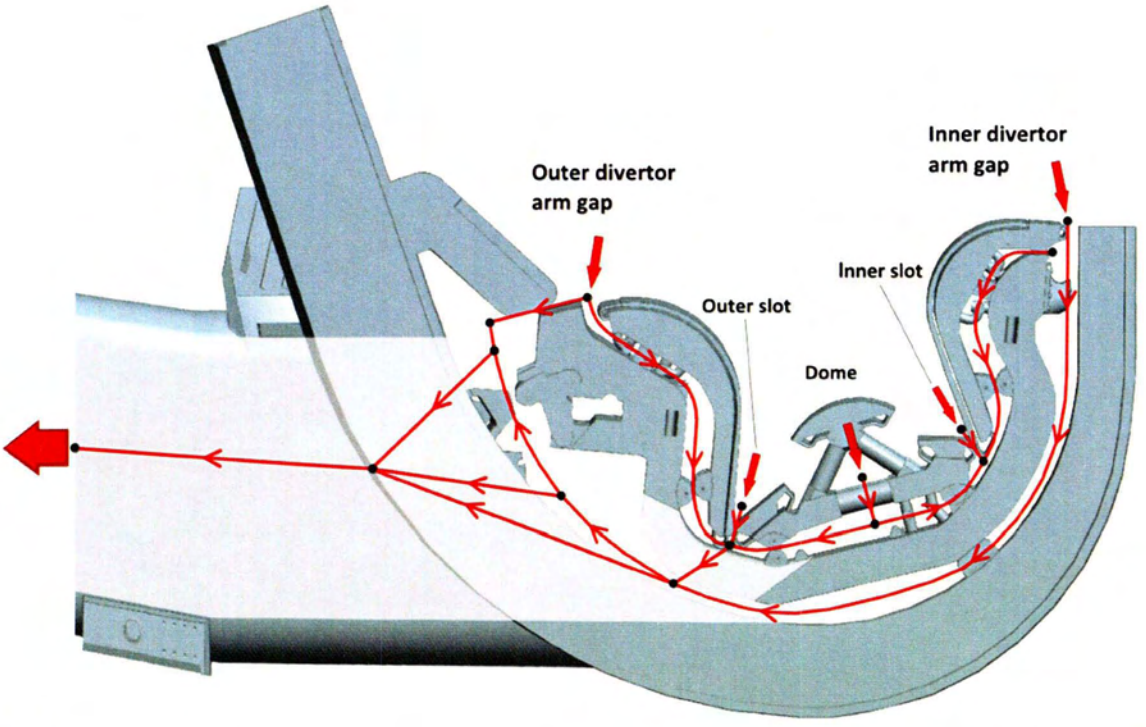

Figure 18: Direction of the gas flow in the pipe network simulating the actual gas flow path in the cross section along a cassette connected to a pump in the dwell phase.

In Fig. 18 the gas flow path in a cross section along a cassette connected with a direct pump is shown. This flow pattern is qualitatively the same in the whole range of pressures investigated in the dwell phase. The gas enters the cassette through all the fixed grade nodes located at the outer and inner divertor arm gaps, outer and inner slots as well as the dome of the cassette. The gas which enters through the upper part of the cassettes flows either to the lower part or towards adjacent cassettes. The gas entering from the lower part though the outer divertor gap of the cassette along with the gas fraction of the upper part, flow toward the pump of the cassette via the three interconnecting ducts. In Fig. 19 the flow path in the gap between adjacent cassettes is shown. It is observed that the gas enters the gap though the four fixed grade nodes and splits into two parts. The one flows immediately to the adjacent cassette through the toroidal connections located at the upper part of the cassette. The other flows downwards and exits the gap through the toroidal connections located at the lower part of the cassette.

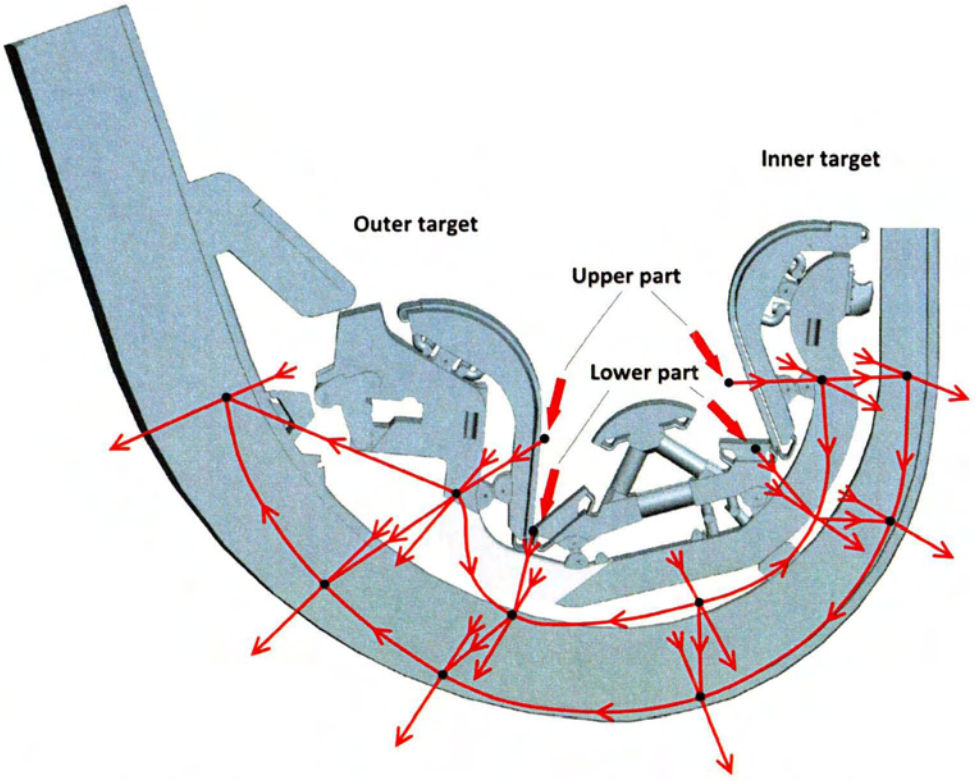

Figure 19: Direction of the gas flow in the pipe network simulating the actual gas flow path between adjacent cassettes in the toroidal direction along the divertor ring and through the gaps between the cassettes facing the plasma side in the dwell phase.

Next, simulation results for the dwell phase scenario are presented in Fig. 20, where the throughputs are plotted in terms of the dome pressure varying between 10^{-5} and 10 Pa with the case of four and six pumps running. The gap between the cassettes is taken 20 mm. Again the throughput is monotonically increased with the dome pressure. With the two additional pumps running the throughput is increased about 50% compared to the case of four pumps at operating (same as in the burn phase). The six pump configuration is mostly considered for the dwell phase where higher throughputs may be needed [50]. The corresponding throughputs in [48] are also included for comparison purposes. They are about 1.5 to 1.8 times higher than the present ones. Once again due to the problem complexity these discrepancies are well within the expected margin errors. It is important to note that again in the dwell phase all the qualitative flow characteristics observed here for the various input geometrical and operational data, are similar to the corresponding ones reported in [48].

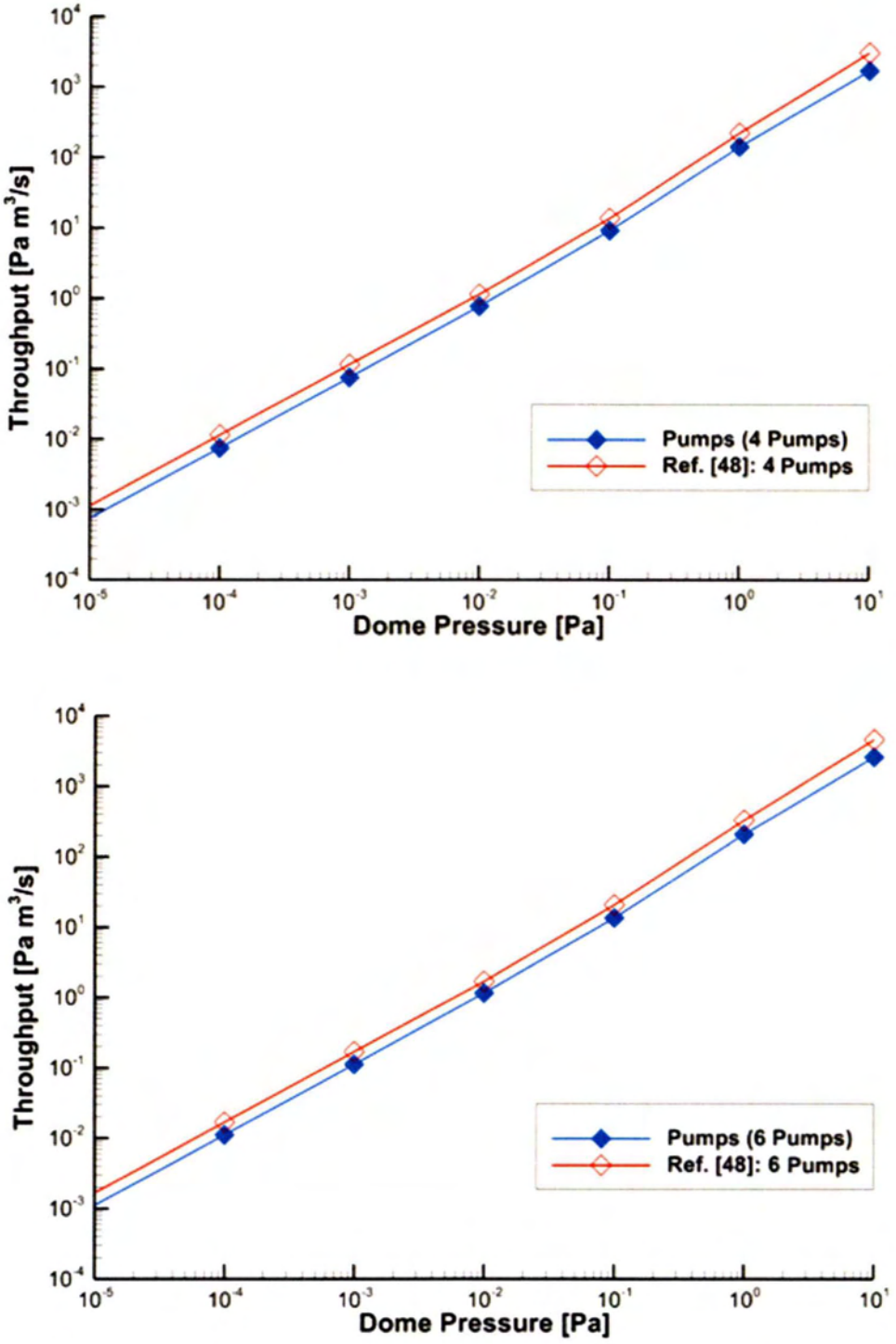

Figure 20: Computed throughputs in the dwell phase versus dome pressure running with 4 (up) and 6 (down) pumps; corresponding results in [48] are also included.

4.2.3 Time-dependent

The ITER vacuum vessel has to be pumped down to a terminal pressure of ≤ 0.5 mPa in the shortest available pumping time being 1400 s. The main gas load during dwell pumping is hydrogen isotopes implanted as energetic particles during the previous DT plasma discharge and thus Deuterium is selected as the conveying gas in the following simulations. From experimental and theoretical studies the outgassing rate from the beryllium wall is found to follow a decay power law with respect to time from an initial outgassing rate. From measurements of outgassing in JET [51] the temporal evolution of the outgassing was found to follow the equation:

$$q_{outgas} = K_1 t^n \tag{4.2.1}$$

where K_1 is the initial outgassing rate in $Pa\,m^3/s$, t is the dwell phase elapsed time and n is the decay index. In order to estimate the initial outgassing rate the procedure described in [52] is followed and is taken as $3.5\,K_1 = Pa\,m^3/s$. The decay index was separately reported as $n = -0.73$ in [51] and as $n = -2/3$ in [53]. In the current study both values of n are examined. The differential equation describing the pressure evolution in the ITER vacuum vessel can be formulated by considering the mass balance as:

$$V\frac{dP}{dt} = K_1 t^n - \dot{m}RT \tag{4.2.2}$$

where V is the vessel volume taken 1400 m^3, T is the temperature of the vessels, R is the conveying gas constant and $\dot{m}$ is the mass flow rate pumped out of the vessel due to the cryopumps. The outgassing from the beryllium wall is assumed to start at 1 s and a typical dome pressure at the end of the burn phase is taken as the initial condition for Eq. (4.2.1):

$$P(1) = 10\ Pa \tag{4.2.3}$$

For the solution of Eq. (4.2.2) the explicit hybrid coupling method described in Chapter 3 is implemented. In Fig. 21 the pressure of the vacuum vessel is shown for an outgassing rate

$K_1 = 3.5\ Pa m^3/s$, a decay index $n = -0.73$ and for 400 K over the course of 1000 s. It is observed that after the first 200 s the pressure evolution is independent from the initial conditions of the vacuum vessel. Thus, it is stated that the quantity of engineering interest i.e. the vacuum vessel pressure at the end of the 1400 s dwell phase is independent from the initial condition given at Eq (4.2.2).

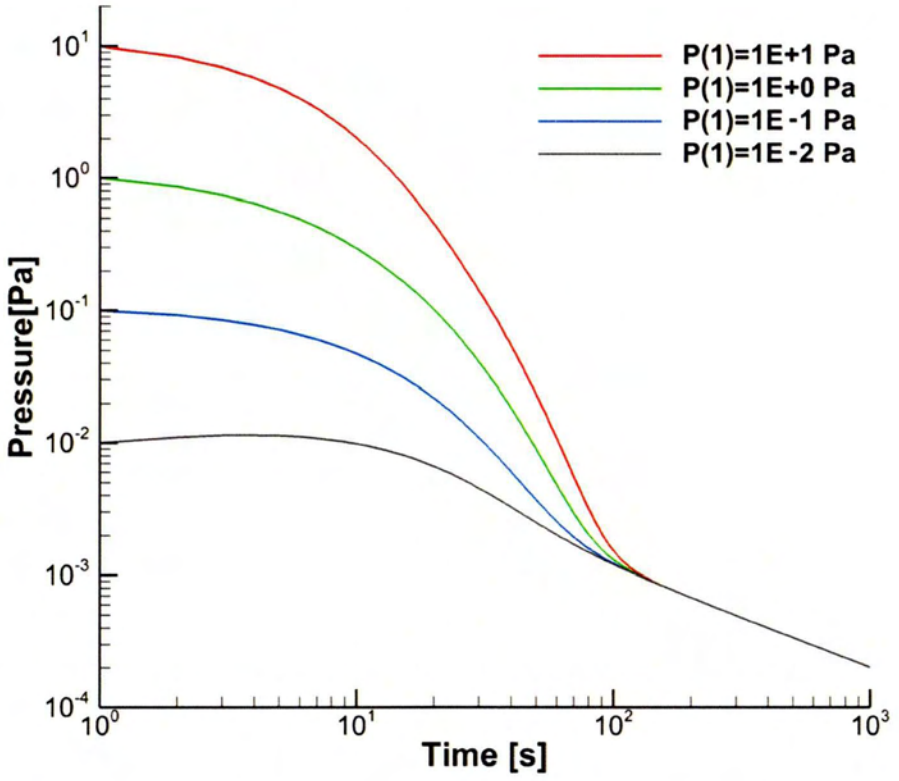

Figure 21: Vacuum vessel pressure distribution over the first 1000 s of the dwell phase for various initial conditions.

In Figs. 22 and 23 the vessel pressure after the 1400 s dwell pumping is presented for various temperature and for $n = -0.73$ and $n = -2/3$. For the simulations two different pumping setups are considered: a) the 4 pump scenario where it is assumed that the cryopumps at ports 4, 6, 10, 12 are running while the pumps located at ports 16 and 18 are regenerating and b) the 6 pump scenario where all pumps are operating. For both decaying indexes it is observed that the end pressure linearly depends on the initial outgassing rate and is decreased as the temperature inside the vessel is increased. In addition, in the case of the six pumps the pressure at the end of

the dwell phase is 33% lower than the four pumps scenario independently of the decaying index and temperature values. In the case of $n = -0.73$ even for an outgassing rate of 10 Pam^3/s which is quite higher than the value expected, the vacuum vessel can be pumped down successfully for all temperatures examined. However, in Fig. 22 it is made clear that the above is not true specifically for the cases of 400 and 600 K.

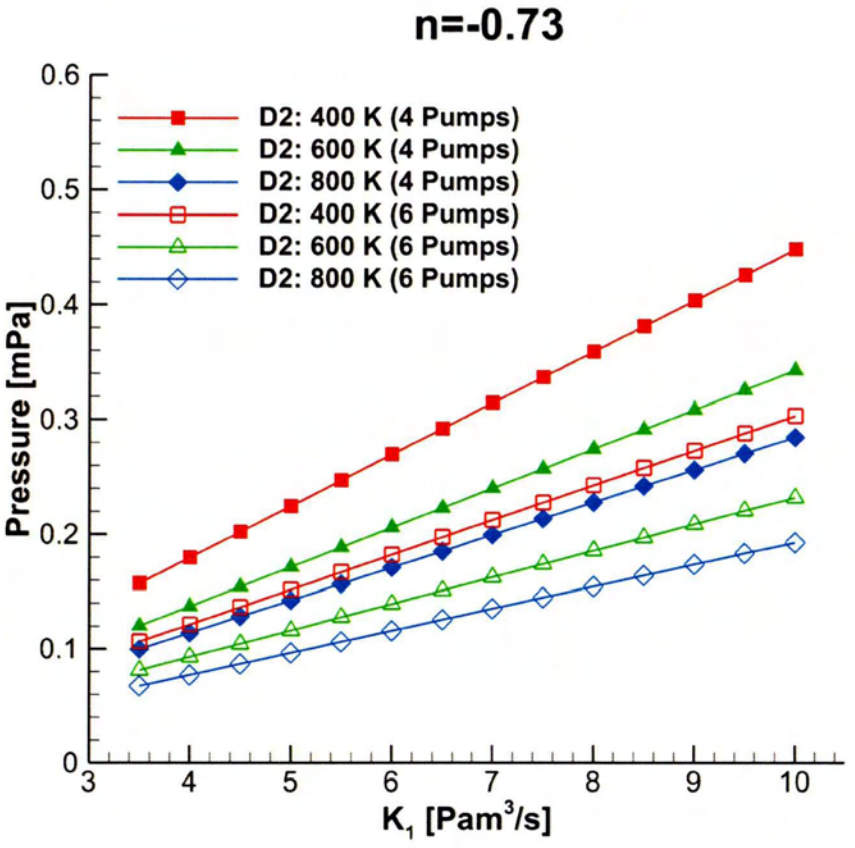

Figure 22: Vacuum vessel pressure at the end of the 1400 s dwell phase versus the initial outgassing rate with a decaying index n=-0.73 for various temperatures and pumping setups.

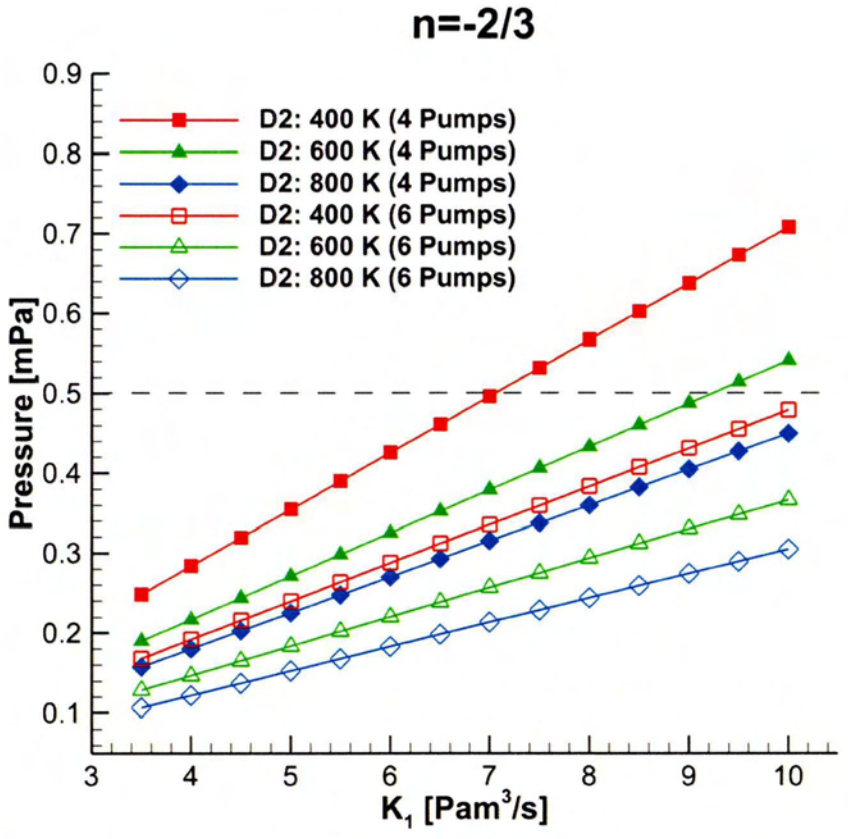

Figure 23: Vacuum vessel pressure at the end of the 1400 s dwell phase versus the initial outgassing rate with a decaying index n=-0.73 for various temperatures and pumping setups.

Chapter 5: Concluding remarks

In the present work an integrated software tool for modeling and simulation of steady-state complex gas distribution systems operating over the whole range of the Knudsen number has been presented and validated. The algorithm's architecture and structure are similar to these of typical hydrodynamic codes, supplemented with a robust kinetic data base in order to provide the required flow rates depending on the geometrical and operational network data. The present work is an extension of a previous algorithm which was limited to relatively small networks that mainly consisted of long channels. The present more advanced and generalized algorithm circumvents these pitfalls by enhancing the kinetic data base to include flow rates through short channels and by implementing an advance subroutine to determine the network loops and pseudoloops. Furthermore a hybrid integration scheme using a data base derived from the steady state code has been suggested and benchmarked for simulating transient networks that consist of up to two finite volume chambers.

In addition, the feasibility and effectiveness of both presented algorithms in simulating large gas networks is demonstrated by simulating the 2012 ITER primary pumping system. Results of the flow patterns and paths along the cassettes and the divertor ring as well as the total throughput for various pumping scenarios and dome pressures are provided. For the steady state results an extensive comparison has been performed with a recent work [41], providing excellent qualitative agreement and satisfactory quantitative agreement taking into account the problem complexity and the different philosophy of the two approaches. The vacuum vessel pressure at the end of the dwell phase has been also estimated for two decaying indexes as well as for various temperatures and outgassing rates and it can be safely assumed that the 1400 s dwell pumping load is manageable.

It is believed that the developed gas distribution network algorithm has a lot of potential in supporting future design work in large vacuum systems of fusion machines and particle accelerators with close collaboration with on-site engineers.

References

[1]: M. Knudsen, Die Molekularstroemung der Gase durch Offnungen und die Effusion, Annalen der Physik, 333(5), 999-1016, 1909.

[2]: Shen Ching, Rarefied Gas Dynamics, Fundamentals, Simulations and Micro Flows, 2005

[3]: Sone, Yoshio. Molecular Gas Dynamics, Theory, Techniques and Applications. 2007.

[4]: G.A. Bird, Molecular Gas Dynamics. 1976.

[5]: Cercignani, C. The Boltzmann equation and its Applications. 1988.

[6]: Bhatnagar P.L., Gross E.P., Krook. M. "A model for Collision Processes in Gases. I. Small Amplitude Processes in Charged and Neutral One-Component Systems." Physical Review (1954): 94(3) 511-525.

[7]: Shakhov, E.M. "Generalization of the Krook kinetic relaxation equation." Fluid Dyn. (1968): 3(5) 95-96.

[8]: Holway, L.H. Approximation procedure for kinetic theory. PhD thesis, Harvard University, 1963.

[9]: Holway, L.H. "New statistical models for kinetic theory." Physics of Fluids (1966): 9: 1658-1673.

[10]: Rykov, V.A. "Model Kinetic Equations for a Gas with Rotational Degrees of Freedom." Izv. Akad. Nauk. SSSR. Mekh. Zhidk. Gaza. (1975): (6), 701-115.

[11]: McCormack, F.J. "Construction of linearized kinetic models for gaseous mixtures and molecular gases." Physics of Fluids (1973): 16: 2095.

[12]: G. A. Bird, Monte Carlo simulation of gas flows, Annual Review of Fluid Mechanics, 10, 11-31, 1978.

[13]: (https://www.iter.org/)

[14]: F. Sharipov, V. Seleznev, Data on internal rarefied gas flows, J. Phys. Chem. Ref. Data 27 (3) (1998) 657–706.

[15]: F. Sharipov, I. Graur, General approach to transient flows of rarefied gases through long capillaries, Vacuum 100 (2014) 22–25.

[16]: Weissberg HL. End correction for slow viscous flow through long tubes. Phys. Fluids 1962; 5(5):1033e6

[17]: Akinshin VD, Makarov AM, Seleznev VD, Sharipov FM. Flow of a rarefied gas in a plane channel of finite length for a wide range of Knudsen numbers. J Appl Mech Tech Phys 1988; 29(1):97e103.

[18]: Akinshin VD, Makarov AM, Seleznev VD, Sharipov FM. Rarefied gas motion in a short planar channel over the entire Knudsen number range. J Appl Mech Tech Phys 1989; 30(5): 713e7.

[19]: S. Pantazis, D. Valougeorgis and F. Sharipov, "End corrections for rarefied gas flows through circular tubes of finite length", Vacuum, 101, 306-312, (2014).

[20]: Sharipov F. Data on the velocity slip and temperature jump on a gas-solid interface. J Phys Chem Ref Data 2011;40(2). 023101.

[21]: V. A. Titarev, Rarefied gas flow in a circular pipe of finite length, Vacuum, 94, 92-103, 2013.

[22]: S. Pantazis, D. Valougeorgis, Rarefied gas flow through a cylindrical tube due to a small pressure difference, Eur. J. Mech. B. Fluids 38 (2013)114–127.

[23]: S. Varoutis, Oleg Sazhin, D. Valougeorgis, F. Sharipov, Rarefied gas flow through short tubes into vacuum, J. Vac. Sci. Technol., A 26 (2) (2008)228–238.

[24]: S. Varoutis, D. Valougeorgis, F. Sharipov, Gas flow through tubes of finite length over the whole range of rarefaction for various pressure drop ratios, J.Vac. Sci. Technol., A 27 (6) (2009) 1377–1391

[25]: S. Pantazis, Simulation of Transport Phenomena in Conditions Far from Thermodynamic Equilibrium via Kinetic Theory with Applications in Vacuum Technology and MEMS, Volos, University of Thessaly, Greece, 2011, PhD Dissertation.

[26]: S. Misdanitis, S. Pantazis, D. Valougeorgis, Pressure driven rarefied gas flow through a slit and an orifice, Vacuum 86 (11) (2012) 1701–1708.

[27]: S. Pantazis, S. Naris, C. Tantos, D. Valougeorgis, J. Andre, F. Millet, J.P. Perin, Nonlinear vacuum gas flow through a short tube due to pressure and temperature gradients, Fusion Eng. Des. 88 (2013) 2384–2387

[28]: S. Varoutis, J. Lihnaropoulos, D. Mathioulakis, A. Tserepi, D. Valougeorgis, Estimation of the Poiseuille number and of the exact hydraulic diameter in rarefied gas flows through channels of various cross sections, in: First European Conference on Microfluidics (mFlu'08), Bologna, Italy, 2008.

[29]: S. Varoutis, Flows through Channels of Various Cross Sections in the Whole Range of the Knudsen Number Using Deterministic and Stochastic Approaches, University of Thessaly, 2008, Ph.D. Thesis

[30]: M. Xr. Dionisios, Design and optimization of compressible gas networks, 2001, Diploma Thesis.

[31]: Z. Poulakis, Design optimization and damage detection in gas distribution networks with the use of classical and evolutionary algorithms, 2002, Postgraduate Thesis.

[32]: S. Varoutis, Reverse design and optimization of incompressible and compressible networks, 2004, Diploma Thesis.

[33]: M.C. Potter, D.C. Wiggert, Mechanics of Fluids, second ed., Prentice Hall, NewYork, NY, 1997.

[34]: A.J. Osiadacz, Method of steady-state simulation of a gas network, Int. J. Syst.Sci. 19 (1988) 2395 – 2405.

[35]: G.P. Greyvenstein, D.P. Laurie, A segregated CFD approach to pipe network analysis, Int. J. Numer. Methods Eng. 37 (1994) 3685–3705.

[36]: (http://kypipe.com/gas;https://en.wikipedia.org/wiki/Gas networks simulation).

[37]: Pigott, R. J. S., Pressure Losses in Tubing, Pipe and Fittings, Trans. ASME, 72 (1950), p. 679

[38]: R. Kersevan and J. L. Pons, Introduction to MOLFLOW+: New graphical processing unit-based Monte Carlo code for simulating molecular flows and for calculating angular coefficients in the compute unified device architecture environment

[39]: Chr. Day, V. Hauer, G. Class, D. Valougeorgis, M. Wykes, Development of a simulation code for ITER vacuum flows, in: IAEA Fusion Energy Conf., 2006, (http://www.pub.iaea.org/MTCD/ Meetings/FEC2006/it p2-12.pdf).

[40]: N. Deo, Graph Theory with Application to Engineering and Computer Science, Prentice-Hall, Englewood Cliffs, NJ, 1974.

[41]: R. Tarjan, Depth first search and linear algorithms, SIAM J. Comput. 1, no 2, pp. 146-160 (1972).

[42]: M. Vargas, S. Naris, D. Valougeorgis, S. Pantazis and K. Jousten, "Hybrid modeling of time-dependent rarefied gas expansion", Journal of Vacuum Science and Technology, 32 (2), 021602, (2014).

[43]: M. Vargas, S. Naris, D. Valougeorgis, S. Pantazis and K. Jousten, "Time-dependent rarefied gas flow of single gases and binary gas mixtures into vacuum", Vacuum, 109, 385-396, (2014).

[44]: D. Valougeorgis, The friction factor of a rarefied gas flow in a circular tube, Phys. Fluids 19 (9) (2007) 091701.

[45]: S. Varoutis and C. Gleason-Gonzalez, Advanced numerical modeling of the neutral gas flow to the divertor pumping system, Final Report for WP12-IPH-A10-1-1-02, Dec. 2012.

[46]: S. Misdanitis and D. Valougeorgis, Algorithm for simulating pipe networks, Final Report for WP 12-IPH-A10-1-1-04, June 2013.

[47]: S. Misdanitis and D. Valougeorgis, Comprehensive investigation of fuelling and pumping opera- tion properties of tokamaks, Final Report for WP13-IPH-A10-P1-01, Dec. 2013.

[48]: V. Hauer and C. Day, ITER divertor gas flow modelling, Fusion Engineering and Design, 98, 1775-1778, 2015.

[49]: C. Gleason-González, S. Varoutis, V. Hauer, C. Day, Simulation of neutral gas flow in a tokamak divertor using the Direct Simulation Monte Carlo method, Fusion Engineering and Design, 89, 1042–1047, 2014.

[50]: R. J. Pearce, A. Antipenkov, B. Boussier, S. Bryan, M. Dremel, B. Levesy, C. Mayaux, M. Wykes, The ITER divertor pumping system, design evolution, simplification and performance, Fusion Engineering and Design, 88, 809-813, 2013.

[51]: V. Philipps and J. Ehrenberg, "Analysis of outgassing after Joint European Torus discharges under beryllium wall conditions," J. Vac. Sci. Technol. A 11(2), March-April 1993, pp. 437–445.

[52]: M. Wykes, P. Andrew, C. Day, G. Federici, Assessment of the ITER dwell pump-down, 21st IEEE/NPS Symposium on Fusion Engineering, 2005.

[53]: P. Andrew and M. Pick, "Hydrogen retention in the first wall," Journal of Nuclear Materials, 220-222 (1995), pp. 601–605.

Appendix A: Basic definitions in kinetic theory

If we consider a 6 dimensional space (phase space) that describes a gas molecule position $\underline{r} = (\mathrm{x}, \mathrm{y}, \mathrm{z})$ and its molecular velocity $\underline{\xi} = (\xi_x, \xi_y, \xi_z)$ the simplest function that contains the desired information is the distribution function denoted as $f(\underline{r}, \underline{\xi}, t)$.The distribution function is defined as the number of gas molecules that at certain time t have position $\underline{r}$ and velocity $\underline{\xi}$ and obeys the Boltzmann equation. Assuming a monoatomic gas subject to an external force $\underline{\mathrm{F}}(\underline{r}, \mathrm{t})$ per unit mass the position $\underline{r}$ and velocity $\underline{\xi}$ of the gas molecule which does not collide with other molecules will change to $\underline{\xi}' = \underline{\xi} + Fdt$ and $\underline{r}' = \underline{r} + \underline{\xi} dt$ in the time interval dt. In the absence of collisions is clear that:

$$f(\underline{r}', \underline{\xi}', t + dt)\, \mathrm{d}\underline{r}' d\underline{\xi}' = f(\underline{r}, \underline{\xi}, t)\, \mathrm{d}\underline{r}\, \mathrm{d}\underline{\xi} \tag{A.1}$$

The Jacobian of the transformation is equal to one if $\underline{\mathrm{F}}$is independent of $\underline{\xi}$ and thus the following expression holds:

$$f(\underline{r}', \underline{\xi}', t + dt) = f(\underline{r}, \underline{\xi}, t) \tag{A2}$$

If collisions are considered Eq. (A.2) must be altered to:

$$f(\underline{r}', \underline{\xi}', t + dt) = f(\underline{r}, \underline{\xi}, t) + \left(\frac{\partial f}{\partial t} \right)_{coll} dt \tag{A.3}$$

Expanding the left hand side of Eq. (A.3), discarding second order terms and letting dt tend to zero the following equation is obtained:

$$\left(\frac{\partial f}{\partial t} + \underline{\xi} \cdot \frac{\partial f}{\partial \underline{r}} + \underline{\mathrm{F}} \cdot \frac{\partial f}{\partial \underline{\xi}} \right) = \left(\frac{\partial f}{\partial t} \right)_{coll} \tag{A.4}$$

Equation (A.4) is incomplete unless the change rate of the distribution function due to molecular collisions is specified. In the derivation of the Boltzmann equation only binary collisions are taken into account. The collision term is split into two separate terms as:

$$\left(\frac{\partial f}{\partial t}\right)_{coll} = R^{+} - R^{-} \tag{A.5}$$

The first one denoted by R^{+} is the gain of molecules that are outside of $\mathrm{d}\underline{r}\,\mathrm{d}\underline{\xi}$ and will be found in $\mathrm{d}\underline{r}'d\underline{\xi}'$ due to a collision while the second one denoted by R^{-} is the loss of molecules that are initially inside $\mathrm{d}\underline{r}\,\mathrm{d}\underline{\xi}$ and will not reach $\mathrm{d}\underline{r}'d\underline{\xi}'$ due to a collision. To compute the two terms it is worthwhile to examine the configuration of a binary collision as shown in Fig. A.1. Consider two types of molecules (type 1 and type 2) with velocities $\underline{\xi}_1, \underline{\xi}_2$ before the collision velocities $\underline{\xi}_1', \underline{\xi}_2'$ after the collision, described respectively by the distribution functions f_1, f_2, f_1', f_2'. The collision of two molecules is described by the impact parameter b, the azimuthal angle φ and the relative collision velocity before and after the collision denoted by $\underline{g} = \underline{\xi}_2 - \underline{\xi}_1$ and $\underline{g}' = \underline{\xi}_2' - \underline{\xi}_1'$ respectively.

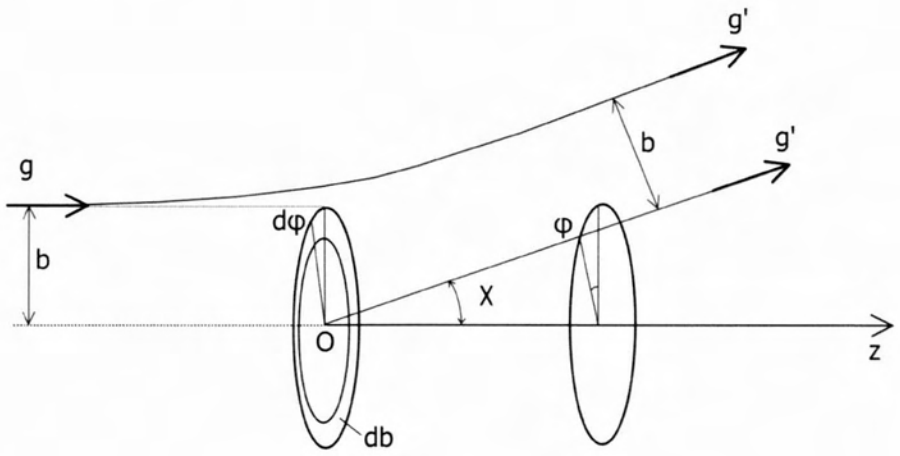

Figure A. 1: Configuration of a binary collision

In the above configuration molecule of type 1 is considered stationary while molecule of type 2 is incident with relative velocity $\underline{g}$ and leaving with velocity $\underline{g}'$. For such a collision to occur in the time interval dt the center of molecules must lie inside a cylinder with volume $gbdtdbd\varphi$. The molecules that are inside the collision cylinder and have velocity $\underline{\xi}_2$ around $d\underline{\xi}_2$ are $f_2 gbdbd\varphi d\underline{\xi}_2 dt$. Such a collision is associated with particles of type 1 with velocity $\underline{\xi}_1$ around $d\underline{\xi}_1$ and thus the expected number of such collisions is $f_1 f_2 gbdbd\varphi d\underline{\xi}_1 d\underline{\xi}_2 d\underline{r}dt$. The type of collisions described above is associated with the loss term R^- which can be now calculated as:

$$R^- = \int\int\int f_1 f_2 gbdbd\varphi d\underline{\xi}_2 \tag{A.6}$$

The gain term can be similarly computed as:

$$R^+ = \int\int\int f_1' f_2' gbdbd\varphi dd\underline{\xi}_2 \tag{A.7}$$

By replacing the collision term in Eq. (A.4) with Eqs. A.6 and A.7 the Boltzmann equation is obtained as:

$$\left(\frac{\partial f_1}{\partial t} + \underline{\xi}\cdot\frac{\partial f_1}{\partial \underline{r}} + \underline{F}\cdot\frac{\partial f_1}{\partial \underline{\xi}}\right) = \int\int\int \left(f_1' f_2' - f_1 f_2\right) gbdbd\varphi d\underline{\xi}_2 \tag{A.8}$$

Because the direct solution of the Boltzmann equation is computationally formidable, suitable kinetic models have been developed that can adequately simulate the collision term. The most widely known and implemented collision model is the BGK kinetic model suggested by Bhatnagar, Gross and Krook in 1954 and is presented here:

$$\left(\frac{\partial f}{\partial t} + \underline{\xi}\cdot\frac{\partial f}{\partial \underline{r}} + \underline{F}\cdot\frac{\partial f}{\partial \underline{\xi}}\right) = v\left(f^M - f\right) \tag{A.9}$$

where v is the collision frequency and f^M is the Maxwellian distribution. A shortcoming of the BGK model is that it cannot provide the correct expressions for both the viscosity and thermal conductivity of the gas.

The solution of either the Boltzmann equation or a suitable kinetic model provides the distribution function in the whole domain, while the macroscopic quantities of interest can be expressed through the distribution. The most common macroscopic quantities are provided:

$$n(\underline{r},t) = \int f(\underline{r},\underline{\xi},t)d\underline{\xi} \tag{A.10}$$

$$u(\underline{r},t) = \int \underline{\xi} f(\underline{r},\underline{\xi},t)d\underline{\xi} \tag{A.11}$$

$$T(\underline{r},t) = \frac{m}{3k\, n(\underline{r},t)} \int \left(\underline{\xi} - u(\underline{r},t)\right)^2 f(\underline{r},\underline{\xi},t)d\underline{\xi} \tag{A.12}$$

$$P(\underline{r},t) = \frac{m}{3} \int \left(\underline{\xi} - u(\underline{r},t)\right)^2 f(\underline{r},\underline{\xi},t)d\underline{\xi} \tag{A.13}$$

Appendix B: Kinetic data for various flow setups

As described in Chapter 2 the infinite capillary theory can be extended from long to medium tubes by introducing the end effect theory. The end effect corrections depend only on the rarefaction parameter of the tube inlet and outlet region and are presented in Table B.1 for completeness.

Table B.1: Length increment $\Delta L / R$ for various values of the rarefaction parameter δ [16]

δ	0.005	0.05	0.1	0.2	0.4	0.6	0.8	1	2
$\Delta L / R$	2.22	1.72	1.52	1.33	1.16	1.07	1.01	0.964	0.841
δ	4	6	8	10	...	∞			
$\Delta L / R$	0.735	0.704	0.688	0.682	...	0.680			

In the case of a pressure driven flow with a small pressure difference ($P_A / P_B > 0.9$) the flow can be considered linear even for short tubes and thus the linear BGK model can be implemented. The flow depends only on the rarefaction parameter and the geometrical ratio of the tube. The solution of the linear problem provides the dimensionless flow rates which are presented for various values of the rarefaction parameter and dimensionless length in Table B.2

Table B.2: Flow rate through a tube for various values of the rarefaction parameter and dimensionless length, based on the linear BGK kinetic model with diffuse boundary conditions [19].

L / R	δ					
	0	0.1	1	2	5	10
0	0.999	1.04	1.37	1.72	2.77	4.35
1	0.672	0.696	0.892	1.10	1.70	2.63
5	0.311	0.316	0.373	0.440	0.642	0.988
10	0.191	0.192	0.217	0.251	0.362	0.554

As described in Chapter 2 in the case $L/R \leq 10$ and $P_A/P_B \leq 0.9$ cannot be considered as linear and the problem must be tackled either with the DSMC method or with suitable nonlinear kinetic models solved by the parallelized discrete velocity method. The nonlinear flow depends on all three flow parameters and the dimensionless flow rate for indicative values of the flow parameters are presented in Table B.3.

Table B.3: Flow rate through a tube for various values of the rarefaction parameter, pressure ratio and dimensionless length, based on the nonlinear ES kinetic model with diffuse boundary conditions.

L/R	P_B/P_A	δ							
		0	0.01	0.1	1	2	5	10	20
0	0.1	0.900	0.903	0.923	1.07	1.18	1.35	1.45	1.50
	0.5	0.500	0.502	0.518	0.653	0.778	1.04	1.22	1.30
	0.9	0.100	0.100	0.105	0.140	0.176	0.280	0.432	0.584
1	0.1	0.605	0.606	0.619	0.713	0.788	0.931	1.06	1.17
	0.5	0.336	0.337	0.345	0.428	0.505	0.692	0.888	1.05
	0.9	0.0672	0.0675	0.0700	0.0908	0.112	0.170	0.264	0.415
5	0.1	0.279	0.280	0.283	0.312	0.341	0.423	0.537	0.701
	0.5	0.155	0.156	0.158	0.182	0.207	0.280	0.398	0.581
	0.9	0.0310	0.0311	0.0318	0.0378	0.0444	0.0641	0.0976	0.164
10	0.1	0.171	0.172	0.173	0.185	0.200	0.249	0.328	0.462
	0.5	0.0954	0.0955	0.0963	0.106	0.119	0.160	0.229	0.359
	0.9	0.0190	0.0191	0.0193	0.0219	0.0253	0.0359	0.0543	0.0917